Spatial beam self-cleaning in multimode lanthanum aluminum silicate glass fiber

Romain Guénard, Katarzyna Krupa, Alessandro Tonello, Fabert Marc, Jean-Louis Auguste, Georges Humbert, Stéphanie Leparmentier, Jean-René Duclere, Sébastien Chenu, Gaëlle Delaizir, et al.

Version of Record: https://www.sciencedirect.com/science/article/pii/S1068520019302445
Manuscript_2684e4e5bf43ddd60578651daf6e8335

Validating the sensitivity of inhomogeneous Magnetization Transfer (ihMT) MRI to myelin with fluorescence microscopy

G. Duhamel[1*], V.H. Prevost[1], M. Cayre[2], A. Hertanu[1], S. Mchinda[1], V. N. Carvalho[1], G. Varma[3], P. Durbec[2], D.C. Alsop[3] and O.M. Girard[1]

[1]Aix Marseille Univ, CNRS, CRMBM - UMR 7339, Marseille, France

[2]Aix Marseille Univ, CNRS, IBDM - UMR 7288, Marseille, France

[3]Department of Radiology, Division of MR Research, Beth Israel Deaconess Medical Center, Harvard Medical School, Boston, MA 02215, USA

***Corresponding author:**

Guillaume Duhamel, PhD

Aix Marseille Univ, CNRS, CRMBM UMR 7339

27 bd Jean Moulin, Faculté de Médecine

13005 Marseille, France

guillaume.duhamel@univ-amu.fr

Highlights

- Inhomogeneous magnetization transfer (ihMT) was validated as a myelin sensitive imaging technique against fluorescence microscopy
- ihMT signal was strongly and significantly correlated with myelin-related plp-GFP (proteolipid - Green Fluorescence Protein) signal
- Short dipolar relaxation time (T_{1D}) filtering is an efficient way to reduce *non*-myelin contribution in ihMT signal
- MT signal was more weakly correlated with plp-GFP signal and had a much larger *non*-myelin contribution
- ihMT contrast can be varied with pulse timing, leading to different signal properties in terms of sensitivity and specificity for myelin content

Data availability statement

Data (Bruker format file) will be shared by request from any qualified investigator.

Abstract

Inhomogeneous Magnetization Transfer (ihMT) is a development from the MT MRI technique. IhMT can be considered as a dipolar order relaxation time (T_{1D}) weighted imaging modality whose signal has shown an enhanced selectivity for myelin-rich structures. However, a formal validation of the ihMT sensitivity relative to a gold standard myelin density measurement has not yet been reported. To address this need, we compared ihMT MRI with green fluorescence protein (GFP) microscopy, in a study performed on genetically-modified *plp-GFP* mice, considered as a reference technique for myelin-content assessment. Various ihMT protocols consisting of variable T_{1D} filtering and radiofrequency power temporal distributions, were used for comparison with fluorescence microscopy. Strong and significant linear relationships (r^2 (0.87-0.96), p <0.0001) were found between GFP and ihMT ratio signals across brain regions for all tested protocol variants. Conventional MT ratios showed weaker correlations (r^2 (0.24-0.78), p ≤0.02) and a much larger signal fraction unrelated to myelin, hence corresponding to a much lower specificity for myelin. T_{1D}-filtering reduced the ihMT signal fraction not attributed to myelin by almost twofold relative to zero filtering suggesting that at least half of the unrelated signal has a substantially shorter T_{1D} than myelin. Overall, these results strongly support the sensitivity of ihMT to myelin content.

R2.1

Key words

Myelin imaging, MRI, inhomogeneous magnetization transfer, ihMT, plp-GFP, fluorescence microscopy

Funding

This work was supported by the national research agency ANR [ANR-17- CE18-0030], VERISMO project.

V. P. received funding from the French Government's 'Investissements d'Avenir' program A*MIDEX, [ANR-11- IDEX-0001-02].

S. M. received funding from ARSEP 2017 grant (Association pour la Recherche sur la Sclérose en Plaques)

V. N. C. received funding from the European Union's Horizon 2020 research and innovation program under the Marie Skłodowska-Curie grant agreement N°713750. Also, it has been carried out with the financial support of the Regional Council of Provence-Alpes-Côte d'Azur and with the financial support of the A*MIDEX (n° ANR- 11-IDEX-0001-02), funded by the Investissements d'Avenir project funded by the French Government, managed by the French National Research Agency (ANR).

1. Introduction

Magnetization transfer (MT) (Wolff and Balaban, 1989) and inhomogeneous Magnetization Transfer (ihMT) (Varma et al., 2015a) are MRI techniques sensitive to the macromolecular content of biological tissues. Whereas conventional MT analysis considers the classic *Zeeman order* magnetization of macromolecules, ihMT highlights *dipolar order* (Varma et al., 2015b), an additional degree of freedom associated to dipolar-broadened lineshapes. Dipolar order corresponds to the polarization of dipolar-coupled spins within their local magnetic fields (Korb and Maruani, 1981; Provotorov, 1962) and is associated with a relaxation time constant, T_{1D}. Relatively long T_{1D} values have been measured in lipid bilayer membranes (Swanson et al., 2017) and in brain white (WM) and grey (GM) matter (Varma et al., 2017). In contrast, much shorter T_{1D}s were estimated in other tissues and samples (Manning et al., 2016; Varma et al., 2015b), which most likely explains the strong selectivity of the ihMT images for myelin-rich structures. This myelin selectivity was further supported by quantitative calculation of the ihMT ratio (ihMTR) values, the ihMT signal normalized by the unsaturated reference signal (S_0): ihMTR~4-10% in GM and WM (Girard et al., 2017, 2015) and ihMTR$\lesssim$1% in muscle tissue (Prevost et al., 2017). In addition to this strong contrast for myelinated tissues, the ihMT technique also benefits from trivial processing, simply based on the subtraction of a minimum of 2 MT images obtained with different radiofrequency (RF) irradiation parameters. Overall, these properties have made ihMT an attractive method to assess myelin-related information *in vivo,* in the clinical context of demyelinating diseases (Rasoanandrianina et al., 2017; Van Obberghen et al., 2018) or in the context of aging studies (Geeraert et al., 2017; Taso et al., 2016). In addition, other studies have shown that the ihMT signal correlates with established myelin-sensitive MR imaging techniques such as myelin water fraction (MWF) (Ercan et al.,

2018; Geeraert et al., 2017). To date, however, no validation of ihMT as a myelin imaging technique against an established histologic standard has been reported.

The existence of an ihMT signal is related to the creation of dipolar order by off-resonance RF irradiation. The ihMT signal is consequently weighted by the associated relaxation time constant T_{1D}. In practice, the sensitization of the ihMT signal for a given T_{1D} value is driven by power and timing parameters of the RF irradiation. Higher RF power tends to increase the ihMT signal of all T_{1D}s (Prevost et al., 2017), but may reduce ihMT contrast by greatly increasing contribution to the signal from short T_{1D} (i.e. few hundreds of μs to ~1ms) components (Manning et al., 2016) relative to longer T_{1D}s (i.e. few ms or longer). Fortunately, when using a train of RF pulses for irradiation, the repetition time of consecutive pulses (Δt) can be tuned to attenuate or filter out the signal contribution from such short T_{1D} components (Prevost et al., 2017). As stressed in recent studies, concentrating RF power within bursts over the long irradiation period, as opposed to RF power regularly distributed along this period, increases the ihMT MRI signal in various tissues (Mchinda et al., 2017; Varma et al., 2018). Overall, the changes in ihMT signal induced by the modification of the irradiation parameters are different depending on the brain structures and type of tissues. Both intensity and contrast in ihMT images depend on the parameters of the RF irradiation, raising additional questions about which acquisitions would correlate best with myelin content. Hence several variants of ihMT acquisitions should be validated against a gold standard myelin measure.

We address this need below by comparing ihMTR values derived from ihMT experiments with different irradiation parameters with myelin-content assessed with a reference technique. Several methods for *ex vivo* myelin visualization and quantification are available, including histochemical Luxol Fast Blue staining (Kluver and Barrera, 1953), Myelin Basic Protein (MBP) immunostaining, myelin fluorescent reporter mice or transmission electron microscopy. Genetically-modified *plp-GFP* (*proteolipid protein-Green Fluorescent Protein*)

mouse is the animal model in which the green fluorescent protein (GFP) is specifically expressed in myelinating oligodendrocytes (Le Bras et al., 2005; Spassky et al., 2001). The GFP fluorescence, which is directly observable and quantifiable with fluorescence microscopy, reflects the expression of proteolipid protein, the major myelin protein in the central nervous system. In the adult brain of these mice, GFP-expressing cells are mature oligodendrocytes but not oligodendroglial progenitors (Ferent et al., 2013). Therefore, fluorescence microscopy performed on *plp-GFP* mice represents a direct and very valuable tool to observe and quantify myelin content. We chose *plp-GFP* fluorescence as the reference technique for validating ihMT as a myelin imaging technique.

R2.2

2. Material and Methods

2.1 Ethics statement

Animal experiments were conducted on C57Bl/6J mice and *plp-GFP* mice and were performed following French guidelines for animal care from the French Department of Agriculture (Animal Rights Division), the directive 2010/63/EU of the European Parliament and of the Council of 22 September 2010 and approved by our institutional committee on Ethics in animal research (Comité d'Ethique de Marseille n°14, project authorization *APAFIS#1747-2015062215062372v6*).

2.2 IhMT technique and irradiation schemes

An ihMT image is generated by the subtraction of an MT image obtained with a single frequency-offset RF irradiation at $+\Delta f$, MT^{+}, and an MT image obtained with a symmetric dual frequency-offset RF irradiation at $\pm\Delta f$, MT^{+-}, both performed with identical average RF power. Single frequency-offset RF irradiation of the macromolecular pool creates dipolar order (Manning et al., 2016; Varma et al., 2015b), which reduces RF saturation effects contributing to the MT^{+} signal. On the other hand, simultaneous symmetric dual frequency-offset RF

irradiation eliminates any dipolar order contribution from the MT^{+-} signal (Varma et al., 2015b) and leads to enhanced RF saturation effects (Swanson et al., 2017). Hence, the (MT^{+} - MT^{+-}) image, that is ihMT, isolates the dipolar order contribution from the MT effects. To minimize sensitivity to off-resonance and asymmetry of the macromolecular line, a second ihMT image using negative frequency irradiation for the single frequency image is also acquired and added to the first (Prevost et al., 2016; Varma et al., 2015a). It has been shown that dipolar order effects are weighted by dipolar relaxation mechanisms (characterized by the dipolar relaxation time T_{1D}) and this additional weighting can be exploited to attenuate/filter out the signal from short T_{1D} components. This is achieved by a modification of the dual frequency-offset RF irradiation experiment, performed sequentially using repetition of frequency alternated RF pulses, as opposed to simultaneously using multiband (e.g. cosine-modulated) RF pulses (Varma et al., 2017). By doing so, dipolar order is allowed to relax in between repeated RF pulses hence providing sensitivity to this contrast mechanism. Based on the above, it may be inferred that the ihMT signal output depends upon the value of T_{1D}, the RF power absorption, and the implementation of the dual frequency-offset RF irradiation. The latter two can be developed to either enhance or attenuate the ihMT signal intensity of components based on their T_{1D} values. The irradiation strategies presented in Fig. 1 were used for this study.

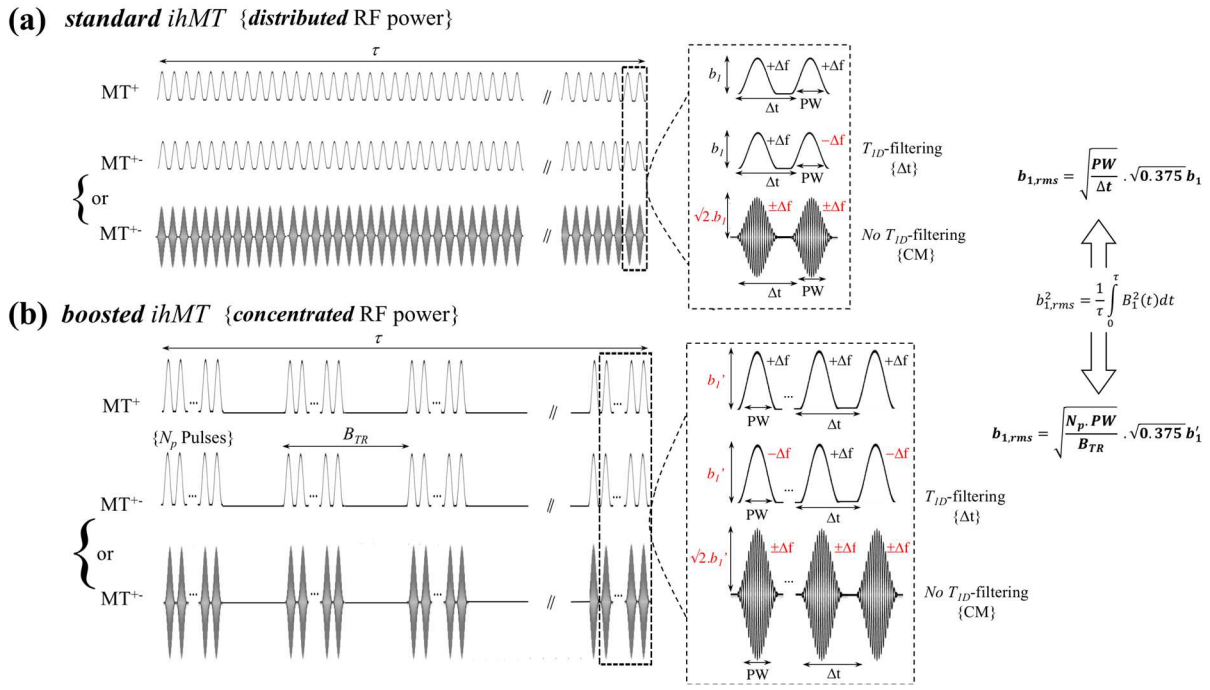

Fig 1. ***Standard* and *boosted* ihMT protocols**. **a)** ***standard*** and **b)** ***boosted*** ihMT protocols obtained with distributed RF power and concentrated RF power throughout the irradiation period, τ, respectively. Concentration of RF power was achieved using bursts of N_p RF pulses followed by a mixing time without RF power, repeated every B_{TR}. Dashed boxes were zoomed in to display the main features of the RF pulses: Hann-shaped pulses (normalized power integral 0.375), duration PW, pulse repetition time Δt, peak power b_1 (standard protocols) or b_1' (boosted protocols), frequency $+\Delta f$ or $-\Delta f$. MT^{+-} was achieved either by frequency alternation (from $+\Delta f$ to $-\Delta f$), allowing T_{1D}-filtering, or with cosine-modulated pulses (CM, peak power increased by a $\sqrt{2}$ factor), producing simultaneous irradiation at $+\Delta f$ and $-\Delta f$. CM pulses did not allow T_{1D}-filtering. Identical irradiation power, $b_{1,rms}$, was used for all experiments. Note that the indicated $b_{1,rms}$ formulas applied for Hann-shape pulses.

The first strategy, referred to as ***standard*** *ihMT* (Fig. 1a) in the following, corresponds to the one used in previous reports of preclinical and clinical studies (Girard et al., 2015; Prevost et al., 2017; Varma et al., 2015a). It employed for RF irradiation, a train of uniformly distributed pulses (peak power, b_1) depositing an average root-mean-square power, $b_{1,rms}$, over the total irradiation time, τ. The second strategy, referred to as ***boosted*** ihMT (Fig. 1b) in the following, employed a concentrated RF power deposition scheme. Bursts of N_p RF pulses followed by relatively long mixing periods (i.e. periods with RF power set off) were repeated every B_{TR} (burst repetition time) for a total irradiation time, τ. Peak power of individual RF pulses (b_1') were adjusted such that the deposited average root-mean-square power was identical to that of

the *standard* ihMT experiment, $b_{1,rms}$. The mixing periods, during which both relaxation and magnetization transfer occur, can be properly tuned to enhance the ihMT signal for a given set of irradiation parameters: In humans, 100-200% ihMT signal increase is possible with $b_{1,rms}$ applied in a concentrated manner rather than with uniform distribution of RF power (Mchinda et al., 2017; Varma et al., 2018).

Dual frequency-offset irradiation of both *standard* and *boosted* ihMT experiments was achieved either sequentially by alternating the offset frequency *(+Δf* to *-Δf)* of consecutive RF pulses or, simultaneously, by using cosine-modulated (CM), i.e. dual-band, shaped pulses. Simultaneous irradiation at $+\Delta f$ and $-\Delta f$ leads to actual decoupling of the dipolar order from the Zeeman order (Varma et al., 2015b) independent of the T_{1D} value. Conversely, the frequency-alternating approach introduces an additional degree of freedom Δt, the time between consecutive pulses, which can be adjusted to modulate the ihMT signal. Fast frequency-alternation ($\Delta t \prec\prec T_{1D}$) averages out dipolar order effects occurring during the individual RF pulses, hence leading to a MT^{+-} signal tending towards the one obtained using the simultaneous CM approach. On the other hand, long Δt values ($\Delta t \succ T_{1D}$) allow dipolar order relaxation to occur between individual RF pulses and leads to a dual frequency-offset irradiation experiment virtually equivalent to the single frequency-offset one for infinitely long Δt values (Varma et al., 2017). For this configuration, the ihMT signal would naturally vanish. In other words, Δt is setting a limit for efficient saturation of both frequency offsets and can be adjusted to attenuate or even filter out the ihMT signal of components associated with short T_{1D} values. Further details of this short $\boldsymbol{T_{1D}}$**-filtering** mechanism can be found in (Prevost et al., 2017).

To summarize, the implementations in Fig. 1 lead to distinct ihMT protocol variants, specifically referred to as the following: *standard* ihMT with or without T_{1D}*-filtering* (Fig 1a)

and *boosted* ihMT with or without T_{1D}*-filtering* (Fig 1b). The value of Δt drives the strength of the T_{1D}-filtering.

2.3 MRI experimental setup

MR experiments were performed with a preclinical 11.75T scanner (Bruker Avance 500 MHz/89 mm wide bore vertical imager, Ettlingen, Germany) and a transmit/receive volume birdcage coil (Bruker, Ettlingen, Germany; length L=3 cm, diameter Ø=2 cm). Experiments were conducted on healthy female C57Bl/6J mice and *plp-GFP* mice. After isoflurane induction in an anesthetic chamber at 3%, mice were maintained under anesthesia during MR experiments by spontaneous respiration of a mixture of air and isoflurane (1.5%; constant flow, 300 mL/min; Univentor 400 anesthesia unit, Zejtun, Malta) through a dedicated nose cone. Respiration and temperature were controlled throughout the experiments with an MR-compatible monitoring and gating system (SA Instruments, Stony Brook, NY, USA). A heating blanket connected to a water bath system was placed on the back of the mice to maintain physiological temperature (T = 37.0 ± 0.5°C).

Prior to ihMT image acquisition, first and second order B_0 shimming was performed using fastmap (Bruker) with a 1.15x1.15x1.15 cm^3 volume centered in the mouse brain. The MT irradiation schemes of Fig. 1 followed by a single-shot RARE (Rapid Acquisition with Relaxation Enhancement) readout were implemented in Bruker's Paravision 5.1 software. The following imaging parameters were used for all experiments: axial orientation; slice thickness, 1 mm; field of view, 20 mm; acquisition matrix, 64 × 64; minimum TE and echo spacing, 1.82 ms; TE_{eff} = 12.74 ms; RARE factor = 38; partial Fourier acceleration = 1.7; linear phase encoding; bandwidth = 400 kHz; acquisition train length ~70 ms; TR = 3 s.

At very high magnetic field, the chemical shift of the macromolecular line induces MT asymmetry effects, which need to be accounted for to obtain reliable ihMT measurements

(Prevost et al., 2016). Compensation was realized experimentally by *i)* shifting the center frequency, f_c, of the irradiation offset-frequency Δf from f_c=*0Hz* to f_c=*-100Hz*, and *ii)* by taking for the single frequency-offset MT image, the average of a MT image obtained with irradiation realized at $f_c+\Delta f$, (MT^+) and one obtained with irradiation realized at $f_c-\Delta f$, (MT^-) *(Prevost et al., 2016)*. Finally, acquisition of two dual frequency-offset MT image (MT^{+-} and MT^{-+}) allows calculation of the final ihMT image as:

$$ihMT = (MT^+ + MT^-) - (MT^{+-} + MT^{-+}) \quad \textit{equation 1}$$

An extra image acquired with the RF irradiation power set to zero, S_0, served as reference signal for normalization and calculation of the semi-quantitative ihMT ratio:

$$ihMTR = \frac{ihMT}{S_0} \quad \textit{equation 2}$$

Single-offset and dual-offset MT ratios ($MTR^{+\Delta f}$ and $MTR^{+/-\Delta f}$) can be derived from the same image dataset as

$$MTR^{+\Delta f} = 1 - \frac{MT^+}{S_0} \quad \textit{equation 3}$$

$$MTR^{+/-\Delta f} = 1 - \frac{MT^{+-}}{S_0} \quad \textit{equation 4}$$

2.4 Validation of ihMT with fluorescence microscopy

This experiment evaluated to what extent ihMTR values obtained with different ihMT protocols correlate with myelin-content. Two axial ihMT RARE slices (position: -0.7mm and -3.2mm from bregma) were acquired on *plp*-GFP mice (n=3, 12 weeks, 23±2g) with six different ihMT variants consisting of both *standard* and *boosted* protocols parameterized with different T_{1D}-filtering strengths: no filtering, achieved by CM; weak filtering; and, strong filtering, the latter two achieved by sequential frequency alternation and increasing values of Δt. The

irradiation parameters of each ihMT variant, summarized in table 1, were chosen to maximize the signal difference between myelinated (WM and GM) and non-myelinated (muscle) structures, based on the results reported in *Prevost et al* (Prevost et al., 2017) for *standard* protocols and on the results of the experiment presented in appendix A for *boosted* protocols. A total number of 80 and 50 repetitions of the ihMT (MT^{+}, MT^{-}, MT^{+-} and MT^{-+}) images were acquired for *standard* protocols and *boosted* protocols respectively. The acquisition time was 3 seconds for a single-NEX MT image and hence 12 seconds for a single-NEX ihMT image. The acquisition time for the 6 investigated configurations (50 NEX and 80 NEX for the *boosted* and *standard* protocols and S_0 images) was 84 minutes and the total experiment (including animal temperature stabilization, RF coil power and shim adjustment, image localization and acquisition of the ihMT protocols) had a duration of 115-120 minutes.

R2.4

Table 1: Parameters for the ihMT protocols used in studies for comparison with fluorescence microscopy

protocol	***T_{1D}-filtering***	***N_p***	***B_{TR}* (ms)**	***PW* (ms)**	***b_1 or b_1'* (μT)**
standard	Strong (***Δt****=3.3ms)*	N/A	N/A	3	11.4
	Weak (***Δt****=1.3ms)*	N/A	N/A	1	12.4
	No (***CM***, *Δt=1.3ms*) *	N/A	N/A	1	12.4
boosted	Strong (***Δt****=3.3ms)*	12	90	3	17.2
	Weak (***Δt****=1.3ms)*	12	90	1	29.8
	No (***CM***, *Δt=1.3ms*)	12	90	1	29.8

S*tandard* and *boosted* ihMT protocols with 3 different T_{1D}-filtering strengths were applied on 3 plp-GFP mice. *PW* corresponds to the pulse length, Δt to the repetition time of consecutive pulses, N_p to the number of pulses per burst, B_{TR} to the repetition time of consecutive bursts and b_1' to the peak-power of the irradiation pulses. The * symbol indicates that the standard protocol without T_{1D}-filtering was applied on 2 mice only. Other irradiation parameters were $b_{1,rms}$=6.7μT, Δf=10kHz and τ=900ms.

After *in vivo* MR experiments, mice were deeply anesthetized (ketamine 150 mg/kg with xylazine 15 mg/kg) and perfused (intra-cardiac) with the fixative paraformaldehyde (PFA) 4%. Mouse brains were then extracted, post-fixed 2 hours in 4% PFA and cryopreserved overnight in 20% sucrose. Brains were frozen and carefully sectioned into 20-μm thick histological slices (Cryostat Leica CM3050S) targeting the same axial planes as imaged by MRI (rostro-caudal levels -0.7mm and -3.2mm from bregma). Sections were mounted with Dabco

anti-fading agent. GFP fluorescence images were acquired using a Zeiss fluorescence microscope with a 5x objective and a fixed exposure time.

2.5 Image processing

MRI data processing was realized with Matlab (vR2012, MathWorks Inc., Natick, MA, USA). For each configuration of table 1, individual 256x256 MT images were reconstructed by Fourier transform after cosine windowing (Harris, 1978) and 4x zero-filling of the 64x64 initial k-space. Magnitude MT images were averaged over the NEX and processed using custom routines to generate the final ihMT and ihMTR images using equations 1 and 2, as well as $MTR^{+\Delta f}$ and $MTR^{+/-\Delta f}$ images using equations 3 and 4. Note that strictly-speaking the concept of T_{1D}-filtering does apply for dual-offset frequency irradiation MT and ihMT, but not for single-frequency irradiation MT. For single frequency RF irradiation, weak and no T_{1D}-filtering experiments were identical (single-offset RF pulses repeated every (Δt=1.3ms)). However, for consistency in presentation, we refer to the different T_{1D}-filtering conditions for ihMTR, $MTR^{+/-\Delta f}$, as well as $MTR^{+\Delta f}$.

Quantitative analyses were performed in 7 different brain structures: internal capsule (IC), corpus callosum (CC), optic nerves (ON), thalamus (Th), cortex (Cx), hippocampus (HC) and Inter-Peduncular Nucleus (IPN). Regions-of-interest (ROIs) were manually placed in these 7 brain structures on ihMTR and GFP fluorescence images (Fig. 3d) by two different observers (V.H.P and M.C) using a mouse brain atlas as reference. The analysis was restricted to these structures, considered relatively homogeneous throughout the 1mm-thick slices, in order to limit partial volume effects in MRI measurements. Mean values of ihMTR, $MTR^{+\Delta f}$ and $MTR^{+/-\Delta f}$ were measured in each ROI for all mice. Quantification of myelin content in each ROI was obtained by measuring the mean GFP fluorescence intensity (ImageJ software (NIH)) in 3

20µm-thick histological sections, spaced by 160µm each, hence covering a total thickness of 340µm. Background fluorescence (measured in the lateral ventricle) was subtracted from the mean GFP fluorescence intensity. The resulting signal was normalized, taking as a reference the ROI with the highest GFP signal, and was referred to as $[\overline{GFP}]$ in the following.

2.6 Statistical analyses

Statistical analyses were performed using JMP software (v9.0.1; SAS Institute, Cary, NC).

One-way analysis of variance followed by a Tukey–Kramer HSD test corrected for multiple comparisons was used to test for differences between brain structures for ihMTR values and GFP values. Three groups of structures were considered for such comparison: white matter, obtained by averaging measurements in IC, CC and ON ROIs; mixed structures, obtained by averaging measurements in Th and IPN ROIs; and grey matter obtained by averaging measurements in Cx and HC ROIs.

Pearson's correlation coefficient (r) and linear regression analysis were used to determine associations of the relationship between individual ihMTR values (derived from the 6 variants of table 1) and myelin-content (GFP fluorescence intensity, $[\overline{GFP}]$) across ROIs in IC, CC, ON, Th, Cx, HC and IPN and animals (n=3). Linear regression analysis was also performed for mean ihMTR values in each ROI calculated over the three animals. A correlation coefficient $r>0.7$ ($r^2>0.5$) being considered as significantly strong with P-value<0.05. Significance of differences between Pearson's correlation coefficients for the 6 sequence variants was tested using Fisher's r-to-z transformation and asymptotic z-test. Slopes and intercepts of regression equations were compared between protocol variants using analysis of covariance (ANCOVA) where ihMTR values were used as a dependent variable, GFP fluorescence intensity ($[\overline{GFP}]$) was used as a covariate, and the protocol variant was used as a categorical factor. In addition, the agreement

between ihMT and GFP fluorescence was assessed by a Bland-Altman analysis (Bland and Altman, 1986). IhMTR values in different anatomical structures were normalized with respect to values in IC. Differences between normalized ihMTR values ($[\overline{ihMTR}]$) and $[\overline{GFP}]$ values were then plotted against their averages. Significance of the bias between ihMT and GFP measurements was evaluated using the one sample t-test for the mean difference. The limits of agreement were calculated as the mean difference ± 1.96 standard deviation of the mean difference. Similar correlation analyses with GFP were performed for $MTR^{+\Delta f}$ and $MTR^{+/-\Delta f}$.

3. Results

Representative *standard* and *boosted* ihMTR images obtained at -3.2mm and -0.7mm from bregma with the 6 ihMT protocols outlined in table 1 and showing different intensities and contrasts are displayed in figure 2. Figures 3a and 3b show the good qualitative agreement in the distribution of signal intensity within the brain between ihMTR and GFP fluorescence images: white matter structures including IC, CC and ON presented high intensities whereas GM Cx and HC showed reduced intensities. ROIs within brain structures used for quantitative measurements of ihMTR and GFP fluorescence, and for correlation analyses are displayed in Fig. 3d. Table 2 summarizes the statistics of GFP fluorescence and ihMTR measurements in brain structures. Values of $[\overline{GFP}]$ and ihMTR were found significantly different in all structures (and for all ihMT configurations). Relative contrast values between WM and GM were higher for T_{1D}-filtered ihMTR images (0.52-0.56) compared to non-filtered ones (0.42-0.45). Conversely, the non-filtered ihMTR images provided the highest SNR values. As for CNR, higher values were obtained for weakly-filtered and non-filtered ihMTR images.

Table 2: Quantitative ihMTR and $[\overline{GFP}]$ values in brain structures

		ihMTR (%)					
	T_{1D}-filtering	***GM {Cx, HC}***	***Mixed structures {Th, IPN}***	***WM {CC, IC, ON}***	***Relative Contrast {WM-GM}***	***CNR {WM-GM}***	***SNR***
Standard protocols	Strong (***Δt**=3.3ms*)	2.2±0.1	3.4±0.1 *, *p<.0001*	4.9±0.6 $^{\#}$, *p<.0001*	0.56±0.02	14±2	26±5
	Weak (***Δt**=1.3ms*)	2.8±0.2	4.0±0.2 *, *p<.0001*	5.9±0.5 $^{\#}$, *p<.0001*	0.52±0.05	15±1	32±4
	No (***CM, Δt**=1.3ms*)	4.5±0.5	6.1±0.9 *, *p=.01*	8.1±0.9 $^{\#}$, *p<.005*	0.45±0.04	15±5	37±7
Boosted protocols	Strong (***Δt**=3.3ms*)	2.6±0.3	4.2±0.4 *, *p<.0001*	6.0±0.6 $^{\#}$, *p<.0001*	0.56±0.05	17±3	34±7
	Weak (***Δt**=1.3ms*)	4.6±0.3	6.7±0.4 *, *p<.0001*	9.6±0.8 $^{\#}$, *p<.0001*	0.52±0.01	22±5	50±10
	No (***CM, Δt**=1.3ms*)	8.7±0.6	11.2±0.9 *, *p<.0001*	15.1±1.0 $^{\#}$, *p<.0001*	0.42±0.01	22±1	70±10
		$[\overline{GFP}]$					
		GM {Cx, HC}	***Mixed structures {Th, IPN}***	***WM {CC, IC, ON}***	***Relative Contrast {WM-GM}***		
		0.17±0.02	0.45±0.03 *, *p<.0001*	0.93±0.09 $^{\#}$, *p<.0001*	0.81±0.02		

Mean values ± standard deviation, calculated by pooling the measurements of the 3 mice in Cx and HC ROIs for GM; in Th and IPN ROIs for mixed structures and the measurements in IC, CC and ON ROIs for WM. The relative contrast between WM and GM was calculated as ($ihMTR^{WM}$-$ihMTR^{GM}$)/$ihMTR^{WM}$ for MRI and as ($[\overline{GFP}]^{WM}$-$[\overline{GFP}]^{GM}$)/ $[\overline{GFP}]^{WM}$ for fluorescence. The CNR was calculated as ($ihMTR^{WM}$-$ihMTR^{GM}$)/σ, and the SNR as $ihMTR^{WM}$/σ, with σ, the noise of the ihMTR image. The $^{\#}$ symbol indicates statistical difference (ANOVA, Tukey-Kramer HSD corrected for multiple comparisons) with values in both GM and mixed structures and the * symbol indicates statistical difference with values in GM.

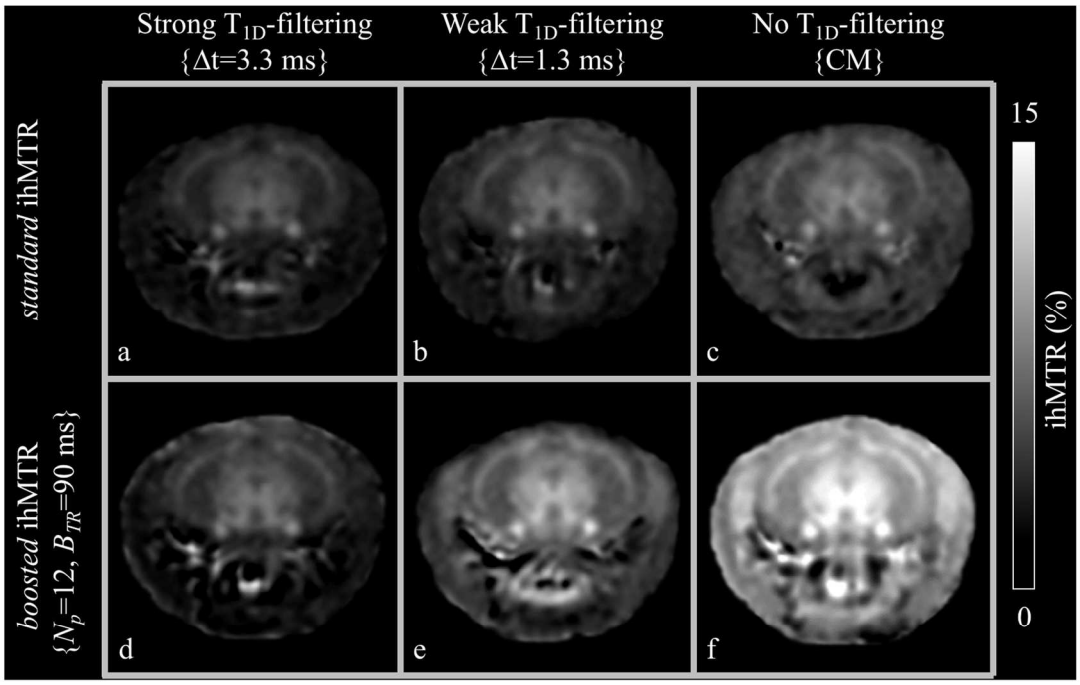

(a) -3.2mm from bregma

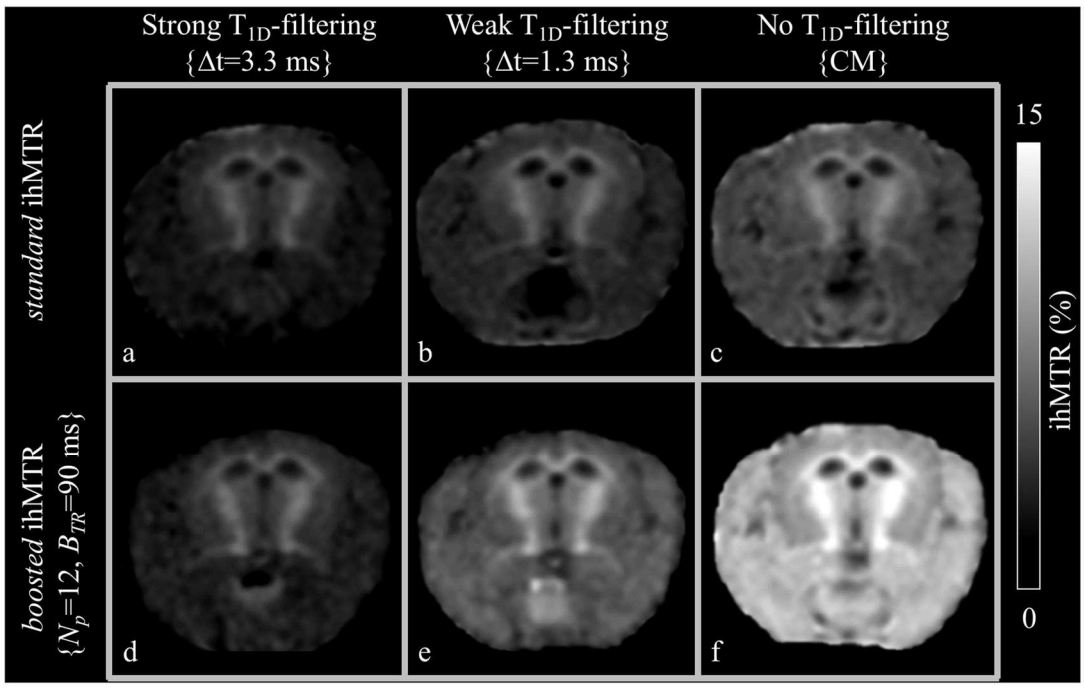

(b) -0.7mm from bregma

Fig 2. *standard* ihMTR and *boosted* ihMTR (N_p=*12*, B_{TR}=*90ms*) maps obtained on the same mouse for different T_{1D}-filtering strengths at **a)** -3.2mm and **b)** -0.7mm from bregma. Other irradiation parameters were $B_{1,rms}$=6.7μT, Δf=10kHz and τ=900ms. These maps were used for correlation analyses with GFP fluorescence by comparing ihMTR values and normalized GFP intensity measured in ROIs outlined in Fig. 3d.

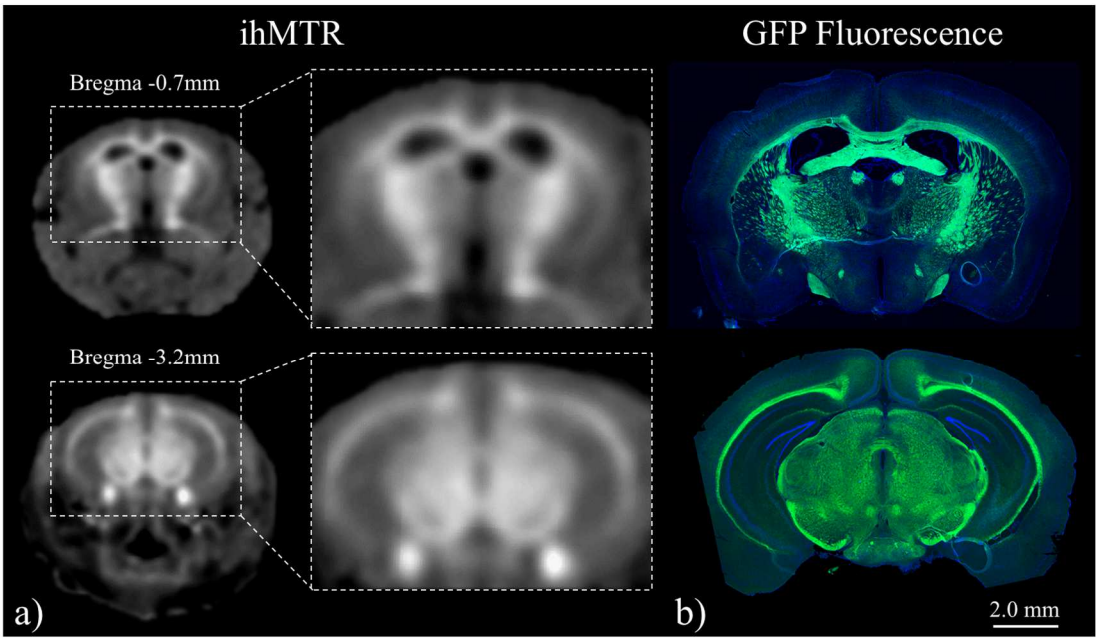
ihMTR
GFP Fluorescence
Bregma -0.7mm
Bregma -3.2mm
a)
b)
2.0 mm

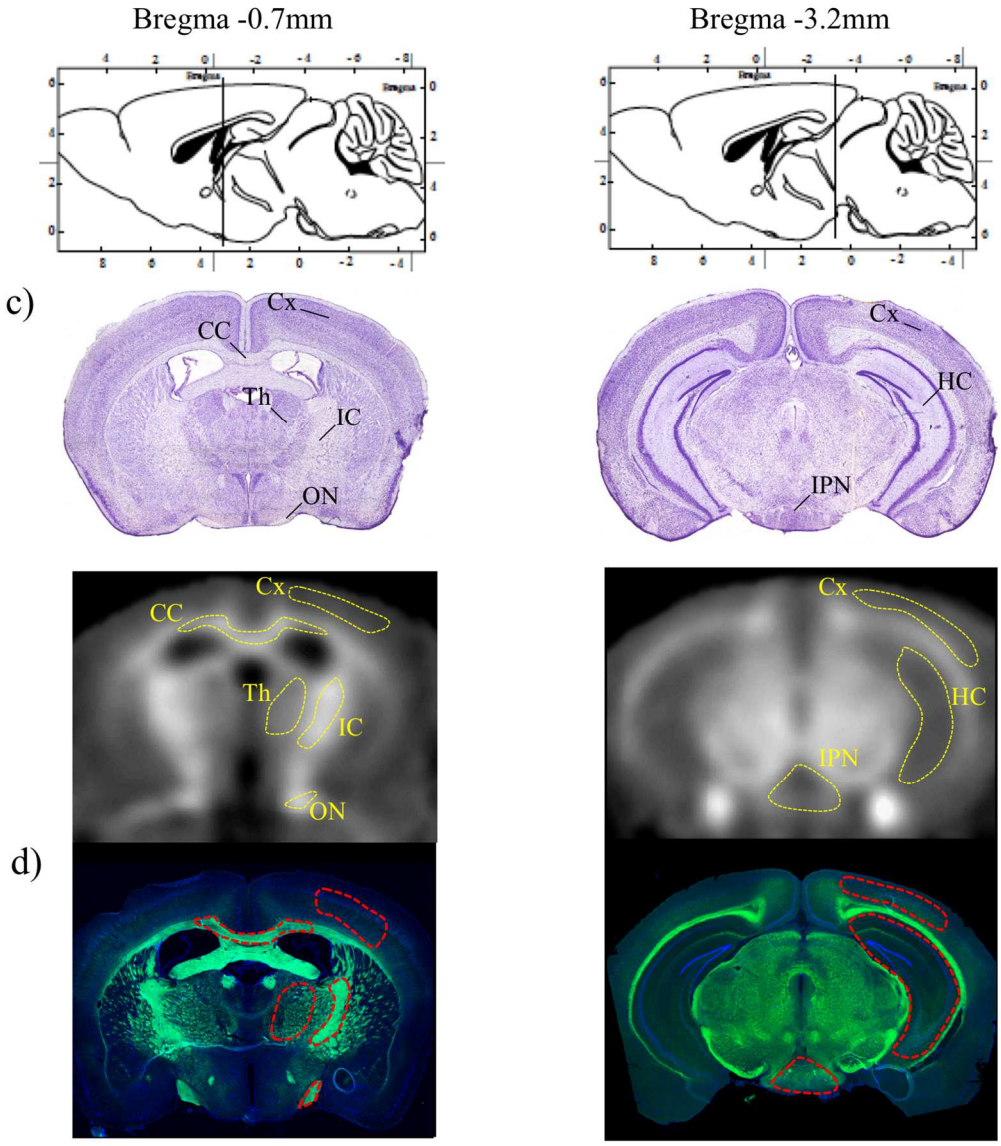
Bregma -0.7mm
Bregma -3.2mm
c)
Cx
CC
Th
IC
ON
HC
IPN
d)

Fig 3. **(a)** ihMTR maps (*boosted* protocol, N_p=*12*, B_{TR}=*90ms*, weak T_{1D}-*filtering*, Δt=*1.3ms*) with insets showing zoomed regions for comparison with **(b)** GFP fluorescence images. Images located at -0.7mm and -3.2mm from bregma. Note that the bright spots visible at the bottom of the ihMTR map (-3.2mm from bregma) correspond to trigeminal nerves, which were not preserved during the brain extraction. **(c)** Mouse brain atlas at -0.7mm and -3.2mm from bregma (Franklin and Paxinos, 2013) indicating the investigated brain structures: cortex (Cx), corpus callosum (CC), thalamus (Th), internal capsule (IC), optic nerves (ON), hippocampus (HC) and Inter-Peduncular Nucleus (IPN). **(d)** ROIs used for quantitative analyses and regression analyses are superimposed on ihMTR maps and GFP fluorescence images.

Results of the linear regression analyses of ihMTR values as a function of the normalized *GFP* signal intensity, $[\overline{GFP}]$, for individual data and averaged across ROIs data are presented in Table 3, and corresponding plots are shown in Figs. 4a and 4b respectively. Bland-Altman plots comparing normalized ihMTR values and normalized GFP intensity in the ROIs are shown in Appendix B (Fig. B.1).

R4

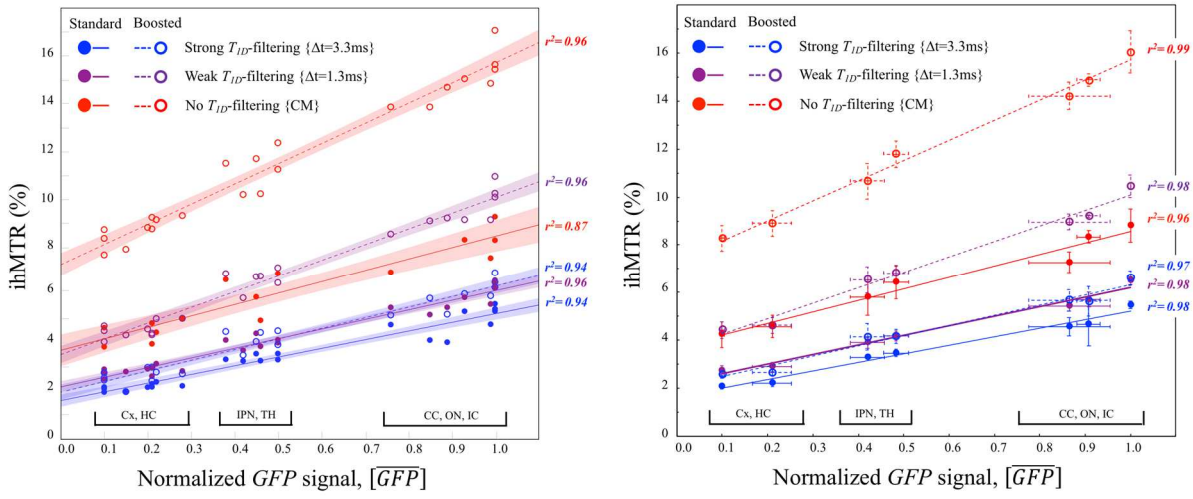

a) b)

Fig 4. Linear regressions of ihMTR values derived from the 6 ihMT protocols described in table 1 on myelin density according to $[\overline{GFP}]$ values in brain structures for **(a)** individual measurements in each animal and each ROI of Figs. 3d and **(b)** mean values in each ROI (error bars representing standard deviations across mice). Plain markers correspond to results from *standard* ihMT protocols (Fig.1a) and open markers from *boosted* ihMT protocols (Fig. 1b). The different colors indicate variable T_{1D}-filtering strengths. Linear fits ($ihMTR = \alpha \times [\overline{GFP}] + \beta$) to scatterplot data were obtained by least-square regression and correlation coefficients, r^2, (assessed by a bivariate (Pearson) correlation test) were reported for all protocols. Shaded areas correspond to confidence curves for line fits with a α–level=0.1. All correlations were significant (p <0.0001).

The significance of the linear relationship between ihMTRs and $[\overline{GFP}]$ ($ihMTR = \alpha \times [\overline{GFP}] + \beta$) was very high for all ihMT protocol variants for both individual data ($0.87 \leq r^2 \leq 0.97$, p <0.0001 (Fig. 4a)) and averaged data ($0.96 \leq r^2 \leq 0.99$, p <0.0001 (Fig. 4b)). Moreover, no significant differences were found for correlation strength of the regression lines between ihMTR variants, thereby validating ihMT as a myelin-sensitive imaging technique, regardless of the selected irradiation parameters. Bland-Altman plots (Fig. B.1) show good agreements between $[\overline{GFP}]$ and $[\overline{ihMTR}]$ for all configurations with a significant bias ranging from ~12% for T_{1D}-filtered protocols to ~20% for non-filtered ones. A proportional bias (~ -0.5) was observed indicating closer agreement for measurements in WM. This proportional bias was reduced for T_{1D}-filtered ihMTR configurations, consistent with the lower intercept obtained from the regression analysis.

R4

Table 3: Linear regression analysis of associations between ihMTR and $[\overline{GFP}]$ – Sensitivity and specificity of ihMTR for myelin.

$ihMTR = \alpha \times [\overline{GFP}] + \beta$										
		T_{1D}-filtering	r	r^2	n	p	$\alpha \pm \delta\alpha, p$	$\beta \pm \delta\beta, p$	$Sp = \frac{\alpha}{\alpha+\beta} \pm \delta Sp$	$NSp = 1 - Sp \pm \delta NSp$
Individual data (Fig. 4a)	*Standard*	Strong (Δt=*3.3ms*)	0.97	0.94	23	<.0001	3.62 ± 0.20, p<.0001	1.60 ±0.12, p<.0001	0.69 ± 0.06	0.31 ± 0.03
		Weak (Δt=*1.3ms*)	0.98	0.96	23	<.0001	4.02 ± 0.19, p<.0001	2.17 ± 0.11, p<.0001	0.65 ± 0.04	0.35 ± 0.03
		No (***CM***, Δt=*1.3ms*)	0.93	0.87	15	<.0001	4.78 ± 0.51, p<.0001	3.70 ± 0.31, p<.0001	0.56 ± 0.08	0.44 ± 0.06
	Boosted ihMT	Strong (Δt=*3.3ms*)	0.97	0.94	23	<.0001	4.43 ± 0.25, p<.0001	1.95 ± 0.15, p<.0001	0.69 ± 0.06	0.31 ± 0.03
		Weak (Δt=*1.3ms*)	0.98	0.96	23	<.0001	6.57 ± 0.28, p<.0001	3.52 ± 0.17, p<.0001	0.65 ± 0.04	0.35 ± 0.02
		No (***CM***, Δt=*1.3ms*)	0.98	0.96	23	<.0001	8.41 ± 0.38, p<.0001	7.29 ± 0.23, p<.0001	0.53 ± 0.03	0.47 ± 0.02
Structure-averaged data (Fig. 4b)	*Standard* ihMT	Strong (Δt=*3.3ms*)	0.99	0.98	7	<.0001	3.56 ± 0.23, p=.0001	1.65 ± 0.15, p<.0001	0.68 ± 0.07	0.32 ± 0.04
		Weak (Δt=*1.3ms*)	0.99	0.98	7	<.0001	3.99 ± 0.23, p<.0001	2.20 ± 0.15, p<.0001	0.65 ± 0.05	0.35 ± 0.03
		No (***CM***, Δt=*1.3ms*)	0.98	0.96	7	<.0001	4.84 ± 0.42, p<.0001	3.74 ± 0.28, p<.0001	0.56 ± 0.07	0.44 ± 0.05
	Boosted ihMT	Strong (Δt=*3.3ms*)	0.99	0.97	7	<.0001	4.28 ± 0.31, p<.0001	2.06 ± 0.20, p=.0002	0.68 ± 0.07	0.32 ± 0.04
		Weak (Δt=*1.3ms*)	0.99	0.98	7	<.0001	6.47 ± 0.35, p<.0001	3.61 ± 0.23, p<.0001	0.64 ± 0.05	0.36 ± 0.03
		No (***CM***, Δt=*1.3ms*)	0.99	0.99	7	<.0001	8.40 ± 0.37, p<.0001	7.33 ± 0.24, p<.0001	0.53 ± 0.03	0.47 ± 0.02

n represents the number of data points used for regression analysis. Sp, calculated as $Sp = \frac{\alpha}{\alpha+\beta}$ corresponds to the component of ihMTR signal associated specifically to myelin and NSp, calculated as $NSp = 1 - Sp = \frac{\beta}{\alpha+\beta}$ to the non-specific signal component; $\delta\alpha$, $\delta\beta$, δSp and δNSp correspond to the standard deviations of each metric. Coefficients of correlation between ihMTR and $[\overline{GFP}]$, r, were assessed by a bivariate (Pearson) correlation test, with $p<0.05$ considered as significant.

Of interest, ihMT was much more highly correlated with myelin, as quantified by GFP, than conventional MTR measurements obtained from the data (Tables S1 and S2 in supplementary materials and corresponding plots shown in Figs. 5): $0.24 \leq r^2 \leq 0.64$, $p < 0.02$ for $MTR^{+\Delta f}$ individual data (Fig. 5a) and $0.47 \leq r^2 \leq 0.69$, $0.02 < p < 0.09$ for $MTR^{+\Delta f}$ averaged data (Fig. 5b); $0.67 \leq r^2 \leq 0.78$, $p < 0.0001$ for $MTR^{+/-\Delta f}$ individual data (Fig. 5c) and $0.73 \leq r^2 \leq 0.82$, $0.03 < p < 0.07$ for $MTR^{+/-\Delta f}$ averaged data (Fig. 5d). Bland-Altman plots (Figs. B.2) show much poorer agreement for $MTR^{+\Delta f}$ and $MTR^{+/-\Delta f}$ with $[\overline{GFP}]$ as compared to ihMTR, with constant biases in the order of ~40-45% and proportional biases 3 times higher (~ -1.5) than those obtained with ihMTR.

R2.5

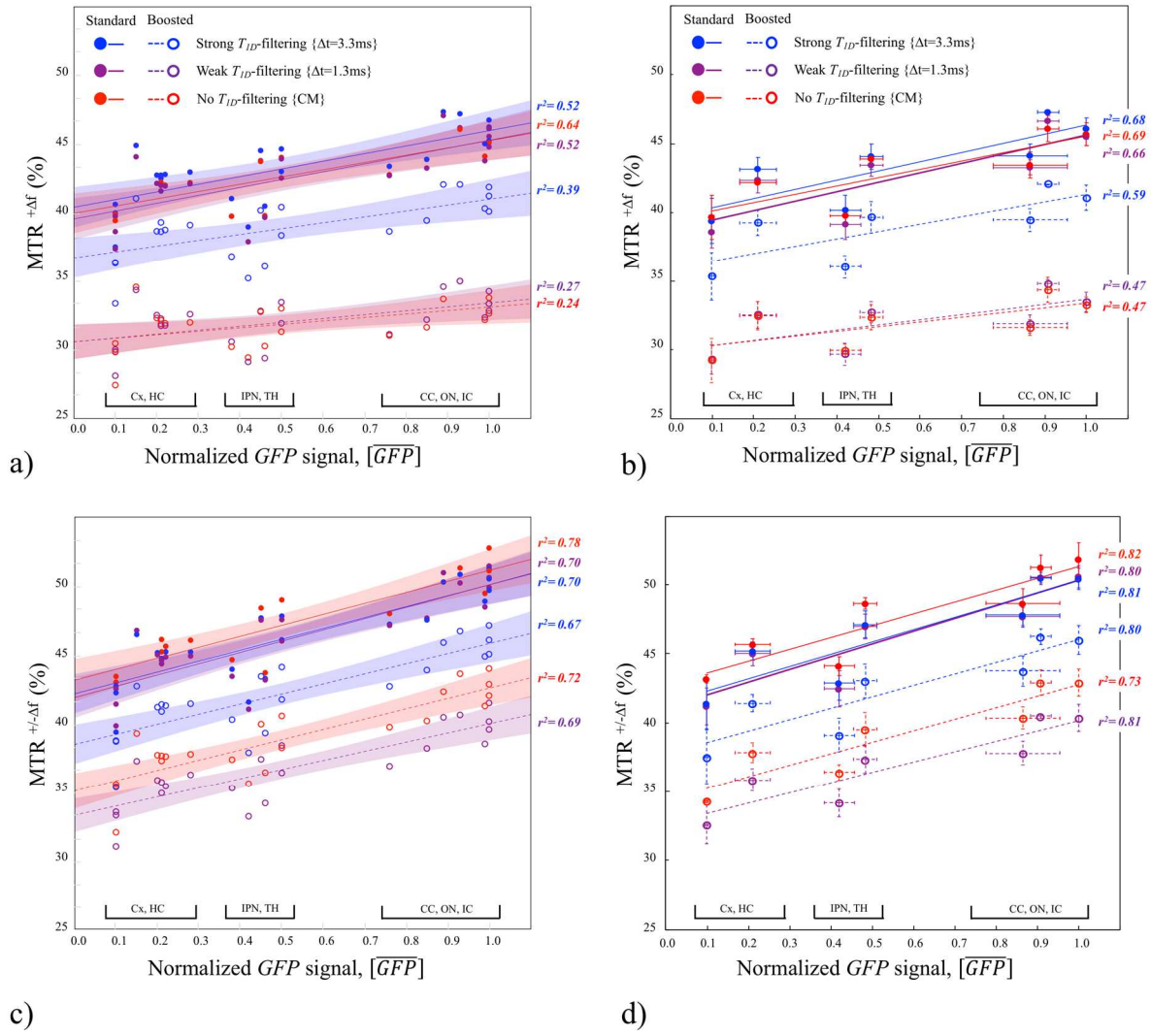

Fig 5: Linear regressions of MTR$^{+\Delta f}$ **(a,b)** and MTR$^{+/-\Delta f}$ **(c,d)** values derived from the 6 protocols described in table 1 on myelin density according to $[\overline{GFP}]$ values in brain structures for **(a, c)** individual measurements in each animal and each ROI of Figs. 3d, and **(b, d)** mean values in each ROI (error bars representing standard deviations across mice). The different colors indicate variable T_{1D}-filtering strengths. Linear fits ($MTR^{+\Delta f} = \alpha \times [\overline{GFP}] + \beta$ **(a,b)** and $MTR^{+/-\Delta f} = \alpha \times [\overline{GFP}] + \beta$ **(c,d)**) to scatterplot data were obtained by least-square regression and correlation coefficients, r^2, (assessed by a bivariate (Pearson) correlation test) were reported for all protocols. Shaded areas correspond to confidence curves for line fits with a α–level=0.1. All correlations were significant (P <0.0001 for MTR$^{+/-\Delta f}$ *v.s.* GFP, and P <0.02 for MTR$^{+\Delta f}$ *v.s.* GFP).

Despite the excellent correlations between ihMTR values and $[\overline{GFP}]$, all ihMT protocol variants are not equivalent. *Boosted* configurations produced significantly higher slope (α) and intercept (β) values (p<0.01) than their counterparts acquired with standard configurations, with the exception of strong-T_{1D} filtering sequences, for which no differences were found in the

intercepts between *standard* and boosted *protocols* (p=0.16). For standard protocols, significant differences in the slopes were found between no T_{1D}-filtering and strong T_{1D}-filtering configurations only (p=0.01), whereas intercepts were different between all T_{1D}-filtering conditions (p<0.03). For boosted protocols, slopes and intercepts were different between all T_{1D}-filtering conditions (p<0.0001). The differences in linear regression α and β parameters provide key information regarding the sensitivity and specificity of ihMTR for myelin. Within the framework of brain tissue analysis, a sensitivity of ihMTR for myelin may be defined by the slope, α, and a corresponding specificity as $Sp = \frac{\alpha}{\alpha+\beta}$. Indeed, for $[\overline{GFP}]$=1 (case of the most myelinated structure taken as reference for normalization), the component of the ihMTR signal associated with this GFP signal (and hence with myelin) is α for a total detected ihMTR signal of $\alpha + \beta$. Hence, *Sp* corresponds to the fraction of the ihMTR signal that is specific to myelin. In other words, $Sp = 70\%$ means that for the most myelinated structure ($[\overline{GFP}]$=1), 70% of the ihMTR signal can be associated specifically with myelin. By extension, one can also define the non-specific ihMTR signal component as $NSp = 1 - Sp = \frac{\beta}{\alpha+\beta}$. The importance of power concentration and T_{1D}-filtering for the sensitivity and specificity of ihMT to myelin is quantitatively highlighted in table 3. Higher slope values (α) obtained with the *boosted* protocols signify higher sensitivity for myelin as compared to their *standard* ihMT variant counterparts. In addition, stronger T_{1D}-filtering resulted in lower sensitivity (lower α) but higher specificity (*Sp*) of ihMTR for myelin. Of particular interest, the myelin-specificity of ihMT is preserved for *boosted* protocols associated with T_{1D}-filtering, as shown by identical values of *Sp* obtained for *standard* and *boosted* ihMT with strong T_{1D}-filtering (*Sp*=0.69±0.06) or weak T_{1D}-filtering (*Sp*=0.65±0.04). Without T_{1D}-filtering, a slight decrease of specificity was observed for *boosted* ihMT (*Sp*=0.53±0.03) compared to *standard* ihMT (*Sp*=0.56±0.08).

The sensitivity of *boosted* ihMTRs was generally higher than that of $MTR^{+\Delta f}$, and for

non-filtered conditions, similar to $MTR^{+/-\Delta f}$. Both $MTR^{+\Delta f}$ and $MTR^{+/-\Delta f}$ were associated with lower values of *Sp,* with minor dependence on the T_{1D}-filtering strengths ($0.08 \leq Sp \leq 0.12$ for $MTR^{+\Delta f}$ and $0.16 \leq Sp \leq 0.18$ for $MTR^{+/-\Delta f}$, Tables S1 and S2 in supplementary material) in comparison to ihMTR.

4. Discussion

4.1 Validation of ihMT with GFP fluorescence microscopy

Notwithstanding the dependence of signal intensity on irradiation parameters, all ihMT protocol variants produced ihMTRs highly correlated with the GFP signal ($r^2 > 0.9$, Fig. 4). Since GFP in our model is expressed under the control of the promoter of *plp*, the major protein constituting myelin, it seems reasonable to assume a linear relationship between GFP signal and myelin content (Le Bras et al., 2005; Spassky et al., 2001), at least in the context of mature and intact myelin. These strong correlations generally validate ihMT as a myelin-sensitive imaging technique. It is important to note that no other correction than the removal of the background noise signal (measured in the ventricle) was applied for calibrating the GFP signal. In particular, the tissue autofluorescence, which may interfere with GFP fluorescence and introduce a signal-offset, was not considered. Since this potential GFP-signal offset would in turn translate into a quantification bias of β, a variability in the absolute values of S_p and NS_p would be expected. However, for a given mouse, since the same GFP-offset bias occurred for all ihMT analyses, the relative differences in α, β, S_p and NS_p observed between the ihMT variants can be generalized.

The validation of ihMT as a myelin-sensitive imaging technique is an important step for the use of ihMT in preclinical and clinical research for diagnosis, therapy follow-up or neuroscience studies.

MT imaging applied in demyelinating disorders showed that MTR variations can be associated with demyelination (Zaaraoui et al., 2008), inflammation (Gareau et al., 2000) and edema (Dousset et al., 1992). The sensitivity of MT to these multiple mechanisms limits the potential of the semi-quantitative MTR parameter to univocally characterize demyelination/remyelination processes in myelin diseases such as multiple sclerosis (Moll et al., 2011). On the other hand, quantitative MT (qMT) provides us with *f*, the macromolecular bound pool fraction (Sled and Pike, 2000), a quantitative metric that is highly-correlated with myelin content in various neurological conditions (Thiessen et al., 2013; Underhill et al., 2011), albeit not specific. The main issue with this model-based technique is the rather long protocol and complex processing (Portnoy and Stanisz, 2007), which requires several parametric images for robust multi-parameter fitting, even for the most optimized ones (Naumova et al., 2017; Yarnykh, 2012).

In contrast, ihMT allows probing an additional degree of freedom within the myelin resonance spectrum and can have an interesting role to play. IhMT variants generally outperformed their conventional MT counterparts for myelin detection, as indicated by much weaker correlations between MTR values and $[\overline{GFP}]$ (Fig. 5). The specificity of ihMTR for myelin was about 4 to 6 times higher than that of $MTR^{+\Delta f}$ and $MTR^{+/-\Delta f}$ (*Sp* values, Tables 3, S1 and S2). The irradiation parameters explored offered limited opportunities to sensitize MT sequences to a specific T_{1D} range for modulation of the myelin-specificity, unlike ihMT protocols. This is demonstrated by the $MTR^{+/-\Delta f}$ data having minor differences in both α and *Sp* for varying MR parameters (table S2, supplementary material), consistent with the dual-frequency offset irradiation being naturally insensitive to T_{1D} because of decoupling of Zeeman order from dipolar order. For single-frequency offset irradiation, although the contribution of dipolar order is embedded in the large MT signal, it may still have an effect: When strong dipolar order is created such as for *boosted* protocols, the sensitivity and specificity for myelin

were reduced (see α and *Sp* in table S1). This is a rather paradoxical situation: the stronger the dipolar order effects are generated in myelinated tissues, the stronger the attenuation of MT^+ saturation effects, hence limiting sensitivity and specificity for these tissues.

Correlations of ihMTRs with myelin histology imaging are as good as those obtained with *f*, the bound pool fraction extracted from qMT analyses (Khodanovich et al., 2017; Underhill et al., 2011), which was found to be the best predictor of pathological myelin content among metrics derived from other advanced MR techniques (DTI, T_1, T_2, MWF) (Thiessen et al., 2013). The intercepts of the linear equations describing the relationship between myelin content and ihMTRs (Fig. 4) and between myelin content and *f* (Thiessen et al., 2013; Underhill et al., 2011) were both non-zero, thereby indicating that structures other than myelin contribute to these measured parameters. Fortunately, with ihMT, T_{1D}-filtering can be used to tailor protocols with variable contributions of non-myelin protons. Although the myelin nonspecific signal component could represent almost half of the total ihMT signal without T_{1D}-filtering, it reduces to a third of the total when modest short-T_{1D} filtering was used (*NSp* values, table 3). This indicates that, on average, ihMT-responding non-myelin protons are associated with T_{1D} values shorter than myelin ones. Though further investigation of the precise nature of those protons is merited, the faster dipolar relaxation of these protons could result from faster water exchange processes (Manning et al., 2016). Hence, membrane protons of less motionally-restricted glial cells, which represent nearly 35% of mouse brain cells (Herculano-Houzel et al., 2006) are reasonable candidates. In principle, even larger Δt values might entirely remove the contribution from short-T_{1D} non-myelin structures, leading to 100% myelin-specific ihMTR images, albeit with lower sensitivity. Note also that further investigation of the contribution of other ihMT parameters (*f*, the fraction of dipolar order associated to T_{1D} and *R*, the exchange rate with the free pool) is merited. Indeed, if the strength of T_{1D}-filtering scales the initial

R2.6

sensitivity, *f* and *R* associated to the different structures may further contribute to the final signal and contrast.

In summary, ihMTRs are semi-quantitative parameters trivial to process, highly correlated to myelin content and whose sensitivity and specificity to myelin can be modulated by sequence parameters variation. These properties are all assets, which warrant future studies to evaluate the potential of ihMT for studies of myelin related disorders.

4.2 What is the optimal ihMT protocol for myelin imaging?

B*oosted* ihMT protocols should benefit all applications of the technique, but the best choice of cosine-modulated pulses or frequency-alternated pulses for dual-offset irradiation would depend on the specific target of the study. Hence, if very high sensitivity (α value) for myelin is sought, then *boosted* ihMT protocols without any T_{1D}-filtering (i.e. use of cosine-modulated pulses), which additionally provide the highest value of SNR and high CNR, are best options. However, the extent to which a significant signal arising from non-myelin protons (*NSp~0.5*, table 3) could interfere with the unambiguous interpretation of ihMTR variations as a change in myelin with this protocol needs to be evaluated. Conversely, protocols with frequency-alternating pulses provide more opportunities to modulate the ihMT contrast with T_{1D}-filtering, offer highest relative contrast values and higher specificity ($Sp \geq 0.65$, table 3) for myelin. As such, b*oosted* ihMT configurations associated with weak T_{1D}-filtering (Δt~1ms), which additionally provide high SNR values and similar CNR than that of non-filtered protocols, can be considered as optimal ihMT protocols.

Interestingly, T_{1D}-filtered and non-filtered ihMT protocols could also be combined together (e.g. by subtraction) to filter-out signal of long-T_{1D} components and modulate specificity for short T_{1D} values. Such short-T_{1D} weighted data would for instance be particularly

interesting in animal models that involve loss of the myelin compact multilamellar structure (e.g. Experimental Allergic Encephalomyelitis (EAE), a relevant model of multiple sclerosis) (Ohler et al., 2004), for which a decrease in T_{1D} values might be expected.

In any case, ihMTR values are not unique for a given tissue but depend on the irradiation scheme and associated parameters. Hence, in order to ease future comparisons, it is recommended to carefully note the type of protocols used, RF irradiation power and T_{1D}-filtering conditions in future reports of ihMT studies.

4.3 Limitations of the study

One of the main limitations of this study is the small number of investigated animals (n=3). Additionally, ihMTR analyses were performed on relatively low resolution and thick slice 2D images, which limited the ability to perform a voxel-by-voxel comparison with GFP images and only permitted the ROI analysis to be performed in a few regions of the brain. Highly resolved 3D imaging and image coregistration would improve the comparison of ihMTR with GFP images. The acquisition time for the multiple NEX used to obtain ihMTR images in this study was rather long, which could prevent their use in multimodal imaging studies. However, halving the number of NEX, and therefore reducing the acquisition time for *boosted* ihMTR images to ~6 minutes, did not change the correlation results (data not shown) nor the conclusions regarding sensitivity and specificity of the ihMTR variants for myelin. This is rather important for human studies, for which a high number of scan repetition is usually not feasible. Finally, no absolute quantification of the measurements was achieved in this study. Hence, even though ihMTR correlates well with GFP fluorescence it does not provide an absolute quantitative measure of myelin content. In this perspective refined quantitative ihMT metrics, including for instance the value of the dipolar order relaxation time, T_{1D}, or the fraction of macromolecules associated to dipolar order, f, could be obtained by application of the ihMT

R2.7

models (Varma et al., 2017, 2015b) on data acquired with several different irradiation parameters.

5. Conclusion

This work reports a formal validation of the ihMT sensitivity relative to a reference myelin density measurement technique, plp-GFP fluorescence microscopy.

All tested ihMT protocol variants, *standard* and *boosted* with or without T_{1D}-filtering, showed very high correlations with GFP detection in the plp-GFP reporter mouse line, thereby generally validating ihMT as a myelin-sensitive technique. Short-T_{1D} filtering reduced the fraction of signal unrelated to myelin, hence making protocols with frequency-alternating pulses for dual-offset frequency irradiation more myelin-specific than those using cosine-modulated pulses.

IhMT protocols generally outperformed their conventional MT counterparts as indicated by higher correlations between ihMTR values and GFP fluorescence signal, 4-6 times higher specificity for myelin, and a broad capacity to sensitize ihMTR to specific T_{1D} ranges. These assets provide motivation for the use of ihMT and to evaluate its potential in future studies of myelin disorders.

6. Appendices

A.1 Characterization of the boosted ihMT protocols

A comprehensive characterization of the *boosted* ihMT protocol is presented and discussed in this *appendix*. It extended analyses of previous studies performed in a clinical context

(Mchinda et al., 2017; Varma et al., 2018) by characterizing the effects of power concentration on the ihMT signal for various T_{1D}-filtering conditions and high RF-power irradiation conditions ($B_{1,rms}$=6.7μT), that are not achievable within typical clinical settings at conventional field strengths ($B_0 \geq 1.5T$). This characterization enabled determining a set of boosted ihMT protocols providing high signal selectivity for myelin-rich structures, which were used for the validation study (section 2.4).

A.2 Methods

Female C57Bl/6J mice (12 weeks, 23±2g) underwent a 2-hour protocol during which axial single-slice (position: -0.7mm from bregma) *boosted* ihMT RARE images (Fig. 1b) were acquired using the parameters in table A1. A total number of 6 mice was necessary to cover the 39 sets of parameters in order to obtain a total number of n=3 mice per parameter set.

Table A1: *boosted* ihMT protocol parameterization

T_{1D}-filtering	***N_p***	***B_{TR}* (ms)**	***PW* (ms)**	***b_1'* (μT)**
Strong (***Δt****=3.3ms)*	6	60, 90, 130	3	19.9, 24.3, 29.3
	12	60, 90, 130	3	14.0, 17.2, 20.7
	18	60, 90, 130	3	11.5, 14.0, 16.9
Weak (***Δt****=1.3ms)*	2	13, 50, 130	1	27.8, 54.4, 87.8
	6	30, 50, 90, 130	1	24.3, 31.4, 42.2, 50.7
	12	30, 50, 90, 130	1	17.2, 22.2, 29.8, 35.8
	18	30, 50, 90, 130	1	14.0, 18.1, 24.3, 29.3
No (***CM***, *Δt=1.3ms*)	2	13, 90, 150	1	27.8, 73, 94.3
	6	30, 50, 90, 130	1	24.3, 31.4, 42.2, 50.7
	12	30, 50, 90, 130	1	17.2, 22.2, 29.8, 35.8
	18	30, 50, 90, 130	1	14.0, 18.1, 24.3, 29.3

Values of variables used for the characterization of the *boosted* ihMT protocol (Fig. 1b) at constant averaged RF irradiation power, $b_{1,rms}$=6.7μT. *PW* corresponds to the pulse length, Δt to the repetition time of consecutive pulses, N_p to the number of pulses per burst, B_{TR} to the repetition time of consecutive bursts and b_1' to the peak-power of the irradiation pulses. Other irradiation parameters were derived from previous optimization of the ihMT signal in brain internal capsule using the *standard* ihMT experiment, Δf=10kHz, and τ=900ms (Prevost et al., 2017). *CM* stands for Cosine-Modulated pulses; Six mice were necessary to cover the 39 sets of parameters with a total number of n=3 mice per parameter set.

For each set of parameters, 20 repetitions of the (MT^+, MT^-, MT^{+-}, MT^{-+}) images were acquired and ihMT processing was realized with the methodology described in the section 2.5. IhMTR values were evaluated in ROIs manually drawn in the internal capsule (IC), cortex (Cx) and muscle (Mu) (Fig. A1) and were further reported as mean in-ROI values ± group (n=3) standard deviation.

A.3 Results

The effect of RF pulse parameters on the ihMT technique is illustrated in Fig. A.1, which shows ihMTR images acquired using the *boosted* ihMT protocol with different levels of RF power concentration and strength of T_{1D}-filtering. Variation of signal intensities and contrasts between long-T_{1D} myelinated WM and GM and shorter-T_{1D} muscle are evidenced depending on saturation parameters. The effect of T_{1D}-filtering can be appreciated by comparing ihMTR images obtained for identical power settings (Fig. A.1b *vs* Fig. A.1c): Strong ihMTR values, albeit non-uniform in all structures, were obtained in the absence of T_{1D}-filtering (use of CM, Fig. A.1c); Use of T_{1D}-filtering attenuated signal in short-T_{1D} muscle, yielding ihMTR images with enhanced contrast between highly-myelinated white matter and muscle (Fig. A.1b). Reducing N_p from 12 to 2 greatly increased ihMTR values in all structures when no T_{1D}-filtering was used (Fig. A.1c *versus* Fig. A.1d) but, significantly reduced them when it was combined with T_{1D}-filtering (Fig. A.1b *versus* Fig. A.1a).

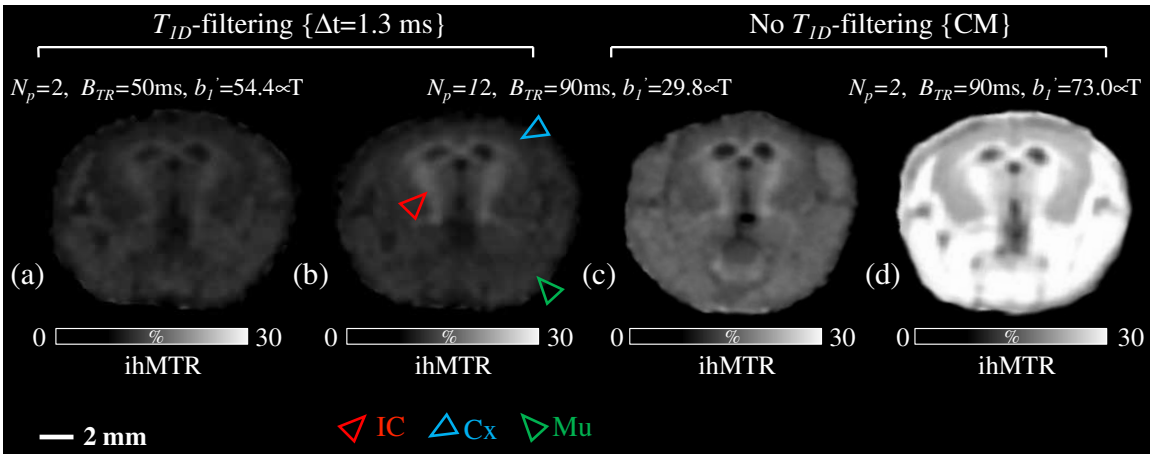

Fig A.1. **Representative *boosted* ihMTR brain images.** IhMTR values and contrasts between structures are modulated by the combined effects of T_{1D}-filtering and the concentration of RF power. Arrows indicate internal capsule (IC, red), cortex (Cx, blue) and muscle (Mu, green). Highly-concentrated RF power (N_p=2) resulted in reduced signal when combined with T_{1D}-filtering **(a)** but in a very large increase without T_{1D}-filtering **(d)**, for which highest ihMTR values were obtained in all brain structures. This highlighted the non-equivalence of frequency-alternated pulses and cosine-modulated pulses for dual-offset irradiation. For less-concentrated RF power, T_{1D}-filtering, **(b)**, allowed better contrast between highly-myelinated WM (e.g. IC) and muscle at the cost of a slight signal decrease compared to that without T_{1D}-filtering, **(c)**.

Figure A.2 shows *boosted* ihMTR values ($ihMTR^{\{boosted\}}$) measured in internal capsule (Figs. A.2a,d,g), cortex (Figs. A.2b,e,h) and muscle (Figs. A.2c,f,i) reported as a function of RF power concentration (driven by both the values of B_{TR} and N_p) and T_{1D}-filtering strength.

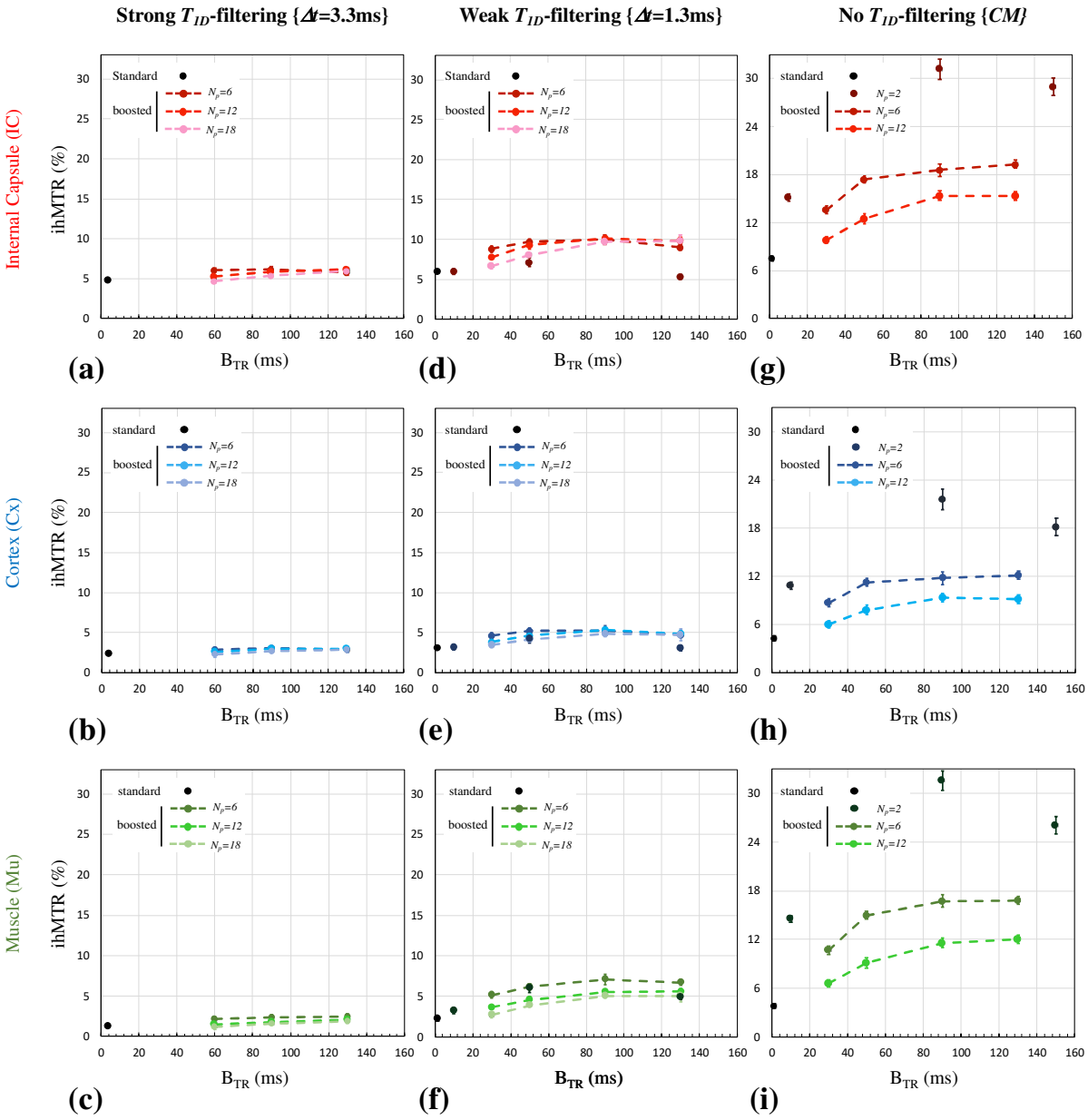

Fig A.2. Dependence of ihMTR with T_{1D}-filtering and RF power concentration. Variations of ihMTR values measured in Internal Capsule (IC, **(a), (d), (g)**), Cortex (Cx, **(b), (e), (h)**) and muscle (Mu, **(c), (f), (i)**) as a function of the T_{1D}-filtering strength (**(a-c)**, strong T_{1D} -filtering, Δt=3.3ms; **(d-f)**, weak T_{1D}-filtering, Δt=1.3ms; **(g-i)**, no T_{1D}-filtering, *CM*) and the RF power concentration (adjusted by variable values of {N_p, B_{TR}}, the number of pulses per burst and the burst repetition time). ihMTR values derived from optimized *standard* ihMT protocols were taken from (Prevost et al., 2017).

For long-T_{1D} tissues, in comparison with the *standard* ihMT protocol, the *boosted* ihMT protocols provided a signal gain (higher ihMTR values) whose magnitude depended on the T_{1D}-filtering strength: whereas the gain was very modest with strong T_{1D}-filtering (Δt=*3.3ms*) (Figs. A.2a,b), the ihMTR signal measured in IC and Cx almost doubled for weak T_{1D}-filtering

(Δt=*1.3ms*) (Figs. A.2d,e) and quadrupled without T_{1D}-filtering (Figs. A.2g,h), as compared to *standard* protocols. Very long B_{TR} values ($B_{TR} \geq$*130ms*) were inefficient as indicated by the onset of decrease of $ihMTR^{\{boosted\}}$ values. RF power concentration from 12 to 2 pulses was inefficient when T_{1D}-filtering was used, leading to decreased ihMTRs.

Boosted ihMT protocols using N_p=*12* and B_{TR}=*90ms* yielded high signal difference between myelin-rich structures and others for all T_{1D}-filtering conditions and were hence chosen for the validation experiment (table 2).

ihMT signal enhancement in short T_{1D}-structures

The three to eight-fold (without T_{1D}-filtering) ihMTR signal increase obtained for muscle tissue, emphasized the stronger signal enhancement of short-T_{1D} tissues using *boosted* ihMT protocols. This effect can be explained by the mechanisms underlying the creation of the ihMT signal, which relies on the influence of dipolar order on RF saturation effects. Exchange of magnetization between Zeeman and dipolar order reservoirs of the bound pool during single-frequency offset irradiation is mediated by the competitive effects of RF power ($R_{rfB} \propto b_1^2$) and dipolar order relaxation (T_{1D}) (Eq. 2 of (Varma et al., 2015b), such that, if dipolar relaxation is too fast, the dipolar order magnetization will remain negligible with no net effect on the RF saturation of the Zeeman magnetization. In this case, the effects of single-frequency offset and dual-frequency offset irradiations would be similar (Eq. 2 tending toward Eq. 3 in (Varma et al., 2015b)), hence resulting in no ihMT effect. A necessary condition for an observable ihMT effect was proposed and formulated by the coarse rule, $R_{rfB}T_{1D} > 0.01$ (Manning et al., 2016). The b_1 values of RF pulses in *standard* ihMT protocols made the previous inequality barely met in short-T_{1D} muscle, hence resulting in reduced ihMTR values. Conversely, concentrating RF pulses at constant average $b_{1,rms}$ such as done in *boosted* ihMT protocols, naturally resulted in pronounced increase of pulse power b_1', thus making the previous inequality met for a broader

range of T_{1D} values, hence revealing ihMT signal from short T_{1D} components. This mechanism likely explains the very large increase of ihMTR in muscle observed, for instance, with *boosted* ihMT protocols and no T_{1D}-filtering (Fig. A.1c).

Non-equivalence of cosine-modulated pulses and frequency-alternated pulses for dual-offset irradiation

The general variations of *boosted* ihMTR values with {N_p, B_{TR}} shown on Fig. A.2 are in agreement with previous experimental results obtained in humans with a 3D steady-state GE sequence and frequency-alternating RF pulses (Mchinda et al., 2017) and with a 2D ihMT prepared sequence with CM RF pulses for dual frequency irradiation (Varma et al., 2018), and are furthermore well supported by the theoretical ihMT model illustrated by numerical simulations (Fig. A.3).

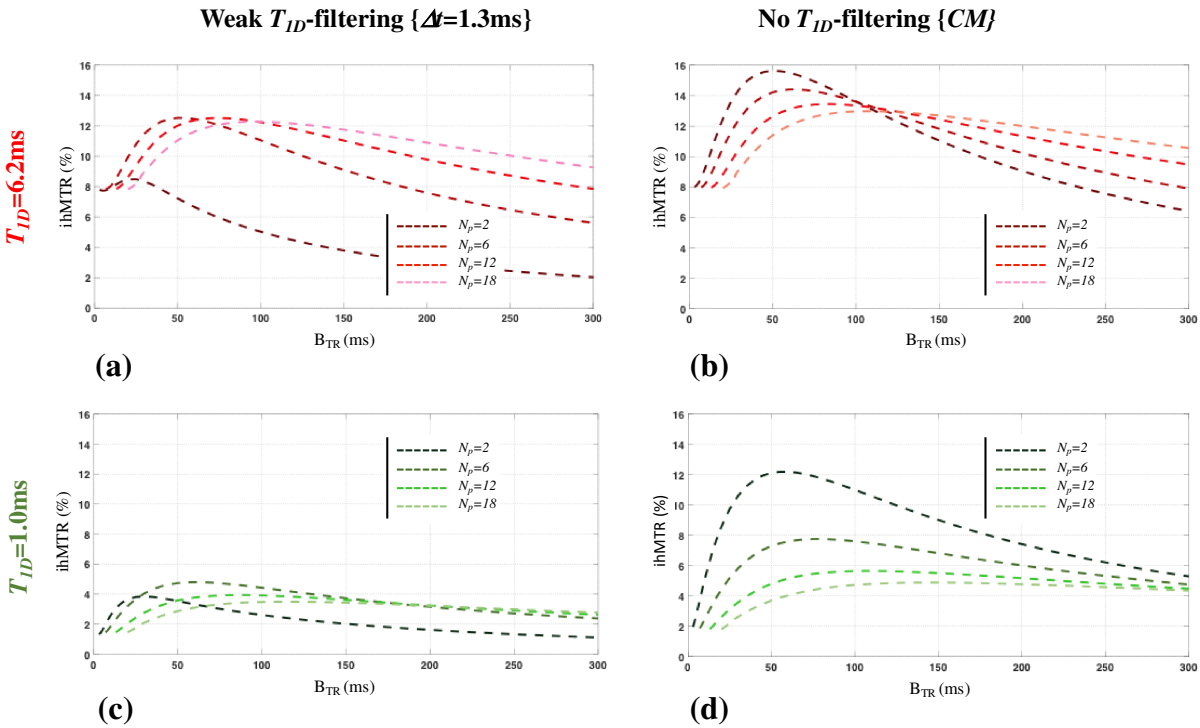

Fig A.3. Numerical simulations of the dependence of ihMTR with RF power concentration with and without T_{1D}-filtering. A piecewise numerical integration of the ihMT theory (Mchinda et al., 2017;

Varma et al., 2015b) was implemented using a MATLAB solver (ode45) and the methodology described in (Mchinda et al., 2017) adapted to the ihMT-prepared *boosted* sequence (i.e. simulating the *boosted* ihMT RARE sequence used experimentally) instead of an ihMT-steady-state *boosted* sequence (i.e. simulating the *boosted* ihMT-GRE sequence). Simulations considered the following tissue parameters, adapted from literature (Mchinda et al., 2017):

$$T_{1A} = 0.65s,\ R = 65s^{-1}, f = 0.65\ , T_{2B} = 12.5\ \mu s,\ 1/(R_{1A}T_{2A}) = 581\ , RM_{0B}/R_{1A} = 7.3$$

Simulations are shown for T_{1D} values of 6.2ms (mimicking Internal capsule case) **(a,b)** and 1.0ms (mimicking muscle) **(c,d)** with weak T_{1D}-filtering **(a,c)** and without T_{1D}-filtering **(b,d)**. RF power concentration was varied with changes in $\{N_p, B_{TR}\}$ values.

This includes: a rapid increase to a maximum, followed by a relatively slower decrease at long B_{TR} values; a higher absolute increase for cosine-modulated based experiments for both long and short T_{1D}s tissues; for short T_{1D}s tissues, a higher relative increase between *standard* ihMT and *boosted* ihMT; and finally, when reducing N_p from 12 to 2, a different variation of ihMTR whether T_{1D}-filtering was used (large decrease, Fig. A.2d and Fig. A.3a), or not (large increase, Figs. A.2g, Fig. A.3b). These opposed variations are important features of *boosted* ihMT protocols performed at high irradiation power, and confirm the major difference between the sequential frequency-alternated pulses and simultaneous cosine-modulated pulses used for the dual-frequency offset irradiation, consistent with previous theoretical predictions (See Fig. 7 of (Mchinda et al., 2017)). The variable efficiency of both approaches for eliminating dipolar order is responsible for this difference as demonstrated by MT simulations (Fig. A.4).

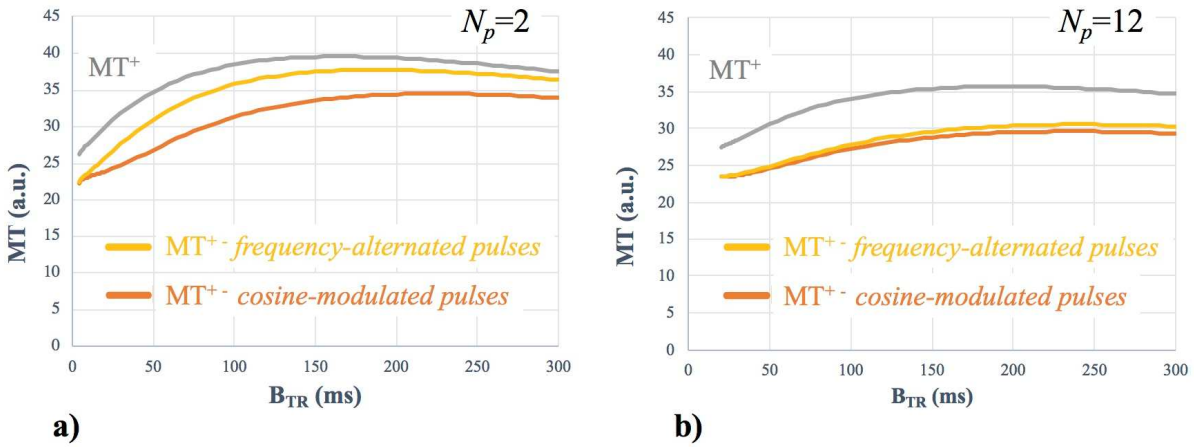

Fig A.4. Numerical simulations of MT⁺ and MT⁺/⁻. Variations of MT⁺ (grey curves) and MT⁺⁻

(achieved with frequency-alternated pulses (yellow curves) and cosine-modulated pulses (orange curves)) with B_{TR} are shown for N_P=2 **(a)** and N_P=12 **(b)**. T_{1D} was set to 6.2ms for both cases. This figure explains the different behavior of frequency-alternated pulses and cosine-modulates pulses for dual irradiation at high RF power concentration, at the origin of the opposed variations of ihMTR for N_P=*2* (Fig. A.2d vs Fig. A.2g, and Fig. A.3a vs Fig. A.3b).

Cosine-modulated pulses, which produce a genuine simultaneous dual-frequency offset irradiation, efficiently decouple Zeeman order from dipolar order independent of the RF pulse power and the T_{1D} value, resulting in a MT^{+-} signal more attenuated than that of MT^{+} (orange curves, Figs. A.4a,b). Conversely, the sequential dual-frequency offset irradiation achieved with the frequency-alternated pulses have similar effects as the simultaneous dual-frequency irradiation only at low pulse-power, as obtained for short B_{TR} and/or high N_p values (yellow curve, Fig. A.4b). Above a certain RF power limit, coupling between Zeeman and dipolar orders induced by an individual RF pulse is too strong to be efficiently compensated and averaged out by the next pulse at the symmetric offset frequency. Hence, sequential dual-offset irradiation progressively tends toward single-offset irradiation, thereby reducing the difference between MT^{+} and MT^{+-} signals (yellow curve, Fig. A.4a), and thus the ihMT signal.

B.1 Bland-Altman Analysis

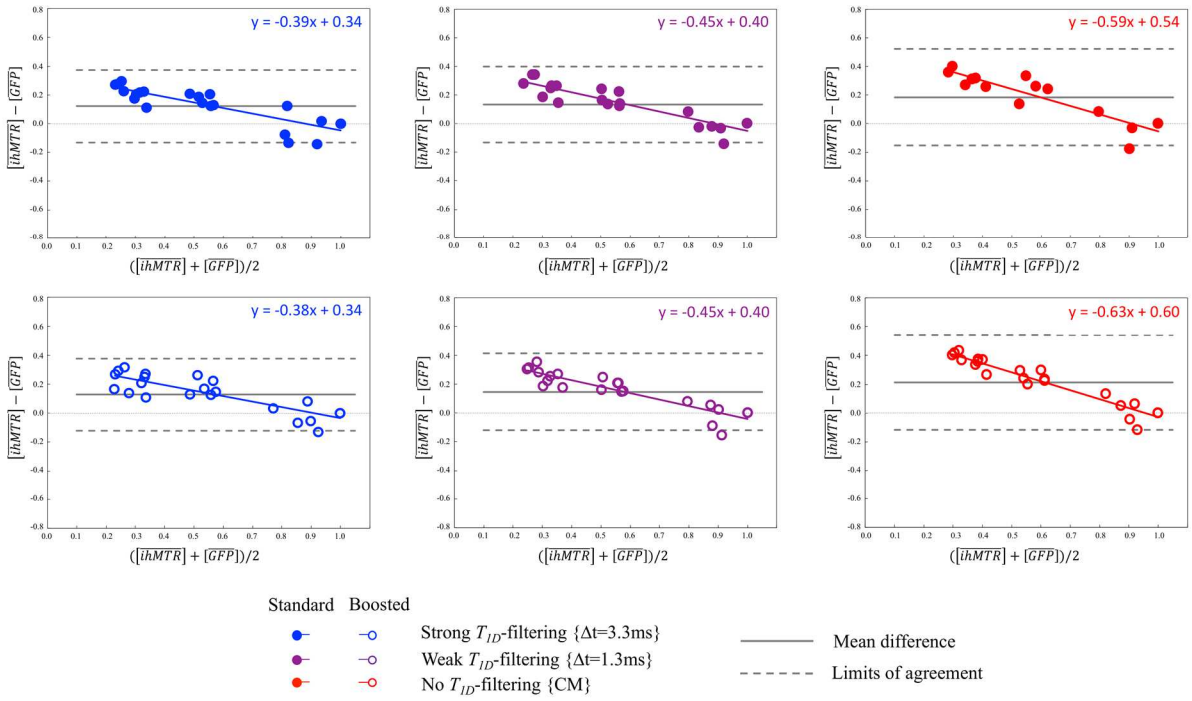

Fig B.1 Bland–Altman plots comparing the normalized ihMTR and $[\overline{GFP}]$ values in IC, CC, ON, Th, IPN, Cx and HC ROIs as illustrated in Figs. 3d. Solid and dashed lines correspond to the mean difference and limits of agreement, respectively.

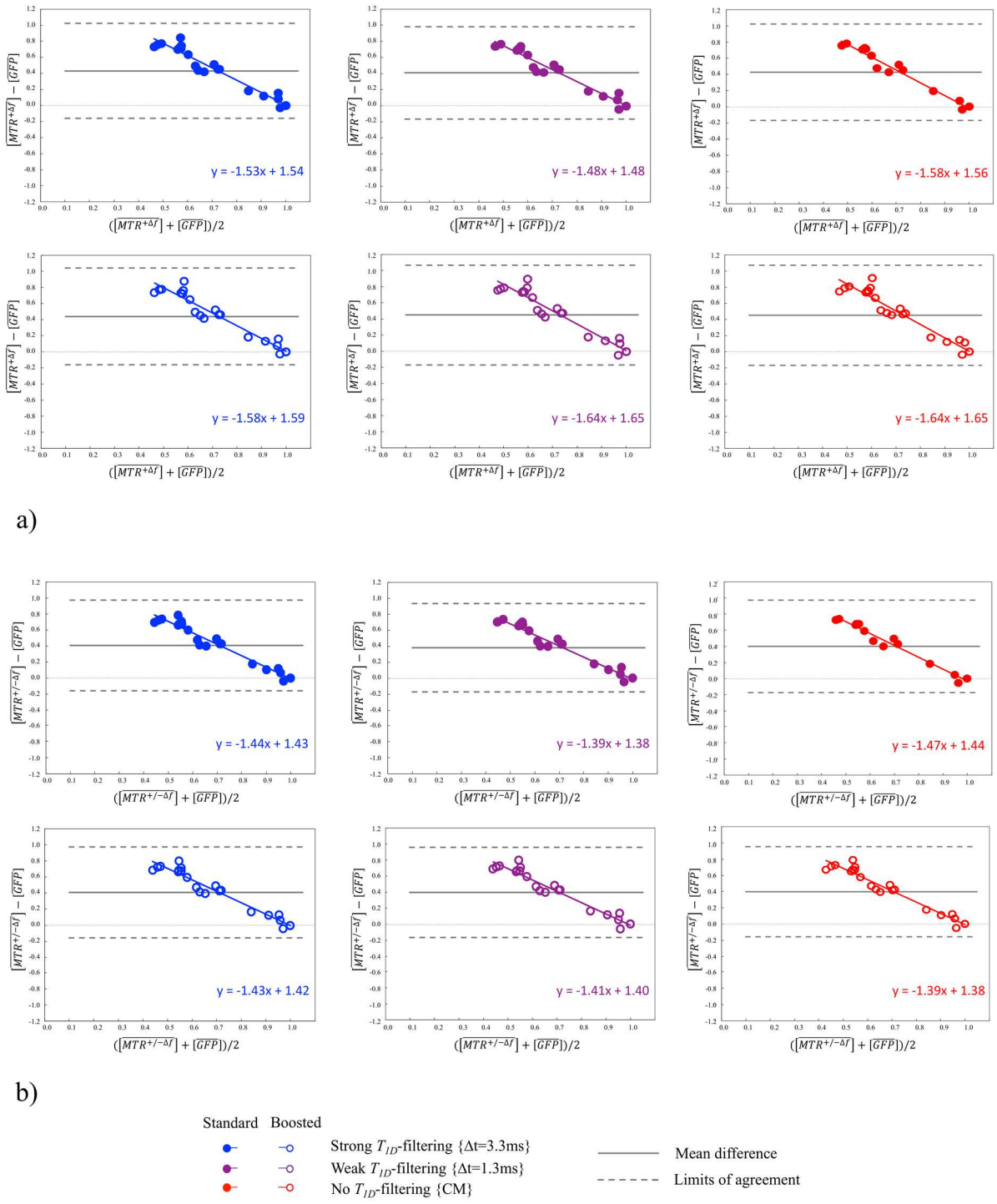

Fig B.2 Bland–Altman plots comparing the normalized MTR$^{+\Delta f}$ and $[\overline{GFP}]$ **(a)**, as well as normalized MTR$^{+/-\Delta f}$ and $[\overline{GFP}]$, **(b),** in IC, CC, ON, Th, IPN, Cx and HC ROIs as illustrated in Figs. 3d. Solid and dashed lines correspond to the mean difference and limits of agreement, respectively.

7. Bibliography

Bland, J.M., Altman, D.G., 1986. Statistical methods for assessing agreement between two methods of clinical measurement. Lancet Lond. Engl. 1, 307–310.

Dousset, V., Grossman, R.I., Ramer, K.N., Schnall, M.D., Young, L.H., Gonzalez-Scarano, F., Lavi, E., Cohen, J.A., 1992. Experimental allergic encephalomyelitis and multiple sclerosis: lesion characterization with magnetization transfer imaging. Radiology 182, 483–491. https://doi.org/10.1148/radiology.182.2.1732968

Ercan, E., Varma, G., Mädler, B., Dimitrov, I.E., Pinho, M.C., Xi, Y., Wagner, B.C., Davenport, E.M., Maldjian, J.A., Alsop, D.C., Lenkinski, R.E., Vinogradov, E., 2018. Microstructural correlates of 3D steady-state inhomogeneous magnetization transfer (ihMT) in the human brain white matter assessed by myelin water imaging and diffusion tensor imaging. Magn. Reson. Med. https://doi.org/10.1002/mrm.27211

Ferent, J., Ruat, M., Traiffort, E., 2013. Investigation of the proteolipid protein promoter activity during demyelination and repair. Differ. Res. Biol. Divers. 85, 182–189. https://doi.org/10.1016/j.diff.2013.05.002

Franklin, K.B.J., Paxinos, G., 2013. Paxinos and Franklin's The mouse brain in stereotaxic coordinates, Fourth edition. ed. Academic Press, an imprint of Elsevier, Amsterdam.

Gareau, P.J., Rutt, B.K., Karlik, S.J., Mitchell, J.R., 2000. Magnetization transfer and multicomponent T2 relaxation measurements with histopathologic correlation in an experimental model of MS. J. Magn. Reson. Imaging 11, 586–595.

Geeraert, B.L., Lebel, R.M., Mah, A.C., Deoni, S.C., Alsop, D.C., Varma, G., Lebel, C., 2017. A comparison of inhomogeneous magnetization transfer, myelin volume fraction, and diffusion tensor imaging measures in healthy children. NeuroImage. https://doi.org/10.1016/j.neuroimage.2017.09.019

Girard, O.M., Callot, V., Prevost, V.H., Robert, B., Taso, M., Ribeiro, G., Varma, G., Rangwala, N., Alsop, D.C., Duhamel, G., 2017. Magnetization transfer from inhomogeneously broadened lines (ihMT): Improved imaging strategy for spinal cord applications. Magn. Reson. Med. 77, 581–591. https://doi.org/10.1002/mrm.26134

Girard, O.M., Prevost, V.H., Varma, G., Cozzone, P.J., Alsop, D.C., Duhamel, G., 2015. Magnetization transfer from inhomogeneously broadened lines (ihMT): Experimental optimization of saturation parameters for human brain imaging at 1.5 Tesla. Magn. Reson. Med. 73, 2111–21. https://doi.org/10.1002/mrm.25330

Harris, F.J., 1978. On the use of Windows for harmonic analysis with the discreteFourier transform. Proc IEEE 66, 51–83.

Herculano-Houzel, S., Mota, B., Lent, R., 2006. Cellular scaling rules for rodent brains. Proc. Natl. Acad. Sci. 103, 12138–12143. https://doi.org/10.1073/pnas.0604911103

Khodanovich, M.Y., Sorokina, I.V., Glazacheva, V.Y., Akulov, A.E., Nemirovich-Danchenko, N.M., Romashchenko, A.V., Tolstikova, T.G., Mustafina, L.R., Yarnykh, V.L., 2017. Histological validation of fast macromolecular proton fraction mapping as a quantitative myelin imaging method in the cuprizone demyelination model. Sci. Rep. 7.

https://doi.org/10.1038/srep46686

Kluver, H., Barrera, E., 1953. A method for the combined staining of cells and fibers in the nervous system. J. Neuropathol. Exp. Neurol. 12, 400–403.

Korb, J.-P., Maruani, J., 1981. Pulse saturation behavior of inhomogeneously broadened lines. II. Rapid-spectral-diffusion case. Phys. Rev. B 23, 5700.

Le Bras, B., Chatzopoulou, E., Heydon, K., Martínez, S., Ikenaka, K., Prestoz, L., Spassky, N., Zalc, B., Thomas, J.-L., 2005. Oligodendrocyte development in the embryonic brain: the contribution of the plp lineage. Int. J. Dev. Biol. 49, 209–220. https://doi.org/10.1387/ijdb.041963bl

Manning, A.P., Chang, K.L., MacKay, A.L., Michal, C.A., 2016. The physical mechanism of "inhomogeneous" magnetization transfer MRI. J. Magn. Reson. San Diego Calif 1997 274, 125–136. https://doi.org/10.1016/j.jmr.2016.11.013

Mchinda, S., Varma, G., Prevost, V.H., Le Troter, A., Rapacchi, S., Guye, M., Pelletier, J., Ranjeva, J.-P., Alsop, D.C., Duhamel, G., Girard, O.M., 2017. Whole brain inhomogeneous magnetization transfer (ihMT) imaging: Sensitivity enhancement within a steady-state gradient echo sequence. Magn. Reson. Med. 79, 2607–2619. https://doi.org/10.1002/mrm.26907

Moll, N.M., Rietsch, A.M., Thomas, S., Ransohoff, A.J., Lee, J.-C., Fox, R., Chang, A., Ransohoff, R.M., Fisher, E., 2011. Multiple sclerosis normal-appearing white matter: Pathology-imaging correlations. Ann. Neurol. 70, 764–773. https://doi.org/10.1002/ana.22521

Naumova, A.V., Akulov, A.E., Khodanovich, M.Y., Yarnykh, V.L., 2017. High-resolution three-dimensional macromolecular proton fraction mapping for quantitative neuroanatomical imaging of the rodent brain in ultra-high magnetic fields. NeuroImage 147, 985–993. https://doi.org/10.1016/j.neuroimage.2016.09.036

Ohler, B., Graf, K., Bragg, R., Lemons, T., Coe, R., Genain, C., Israelachvili, J., Husted, C., 2004. Role of lipid interactions in autoimmune demyelination. Biochim. Biophys. Acta BBA - Mol. Basis Dis. 1688, 10–17. https://doi.org/10.1016/j.bbadis.2003.10.001

Portnoy, S., Stanisz, G.J., 2007. Modeling pulsed magnetization transfer. Magn. Reson. Med. 58, 144–155. https://doi.org/10.1002/mrm.21244

Prevost, V. H., Girard, O.M., Mchinda, S., Varma, G., Alsop, D.C., Duhamel, G., 2017. Optimization of inhomogeneous magnetization transfer (ihMT) MRI contrast for preclinical studies using dipolar relaxation time (T1D) filtering. NMR Biomed. 30. https://doi.org/10.1002/nbm.3706

Prevost, V.H., Girard, O.M., Varma, G., Alsop, D.C., Duhamel, G., 2016. Minimizing the effects of magnetization transfer asymmetry on inhomogeneous magnetization transfer (ihMT) at ultra-high magnetic field (11.75 T). Magn. Reson. Mater. Phys. Biol. Med. 29, 699–709. https://doi.org/10.1007/s10334-015-0523-2

Provotorov, B., 1962. Magnetic resonance saturation in crystals. Zh Exsp Teor Fiz 14, 1126–1131.

Rasoanandrianina, H., Grapperon, A.-M., Taso, M., Girard, O.M., Duhamel, G., Guye, M., Ranjeva, J.-P., Attarian, S., Verschueren, A., Callot, V., 2017. Region-specific impairment of

the cervical spinal cord (SC) in amyotrophic lateral sclerosis: A preliminary study using SC templates and quantitative MRI (diffusion tensor imaging/inhomogeneous magnetization transfer). NMR Biomed. 30. https://doi.org/10.1002/nbm.3801

Sled, J.G., Pike, G.B., 2000. Quantitative Interpretation of Magnetization Transfer in Spoiled Gradient Echo MRI Sequences. J. Magn. Reson. 145, 24–36. https://doi.org/10.1006/jmre.2000.2059

Spassky, N., Olivier, C., Cobos, I., LeBras, B., Goujet-Zalc, C., Martínez, S., Zalc, B., Thomas, J.L., 2001. The early steps of oligodendrogenesis: insights from the study of the plp lineage in the brain of chicks and rodents. Dev. Neurosci. 23, 318–326.

Swanson, S.D., Malyarenko, D.I., Fabiilli, M.L., Welsh, R.C., Nielsen, J.-F., Srinivasan, A., 2017. Molecular, dynamic, and structural origin of inhomogeneous magnetization transfer in lipid membranes. Magn. Reson. Med. 77, 1318–1328. https://doi.org/10.1002/mrm.26210

Taso, M., Girard, O.M., Duhamel, G., Le Troter, A., Feiweier, T., Guye, M., Ranjeva, J.-P., Callot, V., 2016. Tract-specific and age-related variations of the spinal cord microstructure: a multi-parametric MRI study using diffusion tensor imaging (DTI) and inhomogeneous magnetization transfer (ihMT): Spinal Cord Microstructure Assessment Using DTI and ihMT. NMR Biomed. https://doi.org/10.1002/nbm.3530

Thiessen, J.D., Zhang, Y., Zhang, H., Wang, L., Buist, R., Del Bigio, M.R., Kong, J., Li, X.-M., Martin, M., 2013. Quantitative MRI and ultrastructural examination of the cuprizone mouse model of demyelination: MRI IN CUPRIZONE DEMYELINATION. NMR Biomed. 26, 1562–1581. https://doi.org/10.1002/nbm.2992

Underhill, H.R., Rostomily, R.C., Mikheev, A.M., Yuan, C., Yarnykh, V.L., 2011. Fast bound pool fraction imaging of the in vivo rat brain: Association with myelin content and validation in the C6 glioma model. NeuroImage 54, 2052–2065. https://doi.org/10.1016/j.neuroimage.2010.10.065

Van Obberghen, E., Mchinda, S., le Troter, A., Prevost, V.H., Viout, P., Guye, M., Varma, G., Alsop, D.C., Ranjeva, J.-P., Pelletier, J., Girard, O., Duhamel, G., 2018. Evaluation of the Sensitivity of Inhomogeneous Magnetization Transfer (ihMT) MRI for Multiple Sclerosis. AJNR Am. J. Neuroradiol. 39, 634–641. https://doi.org/10.3174/ajnr.A5563

Varma, G., Duhamel, G., de Bazelaire, C., Alsop, D.C., 2015a. Magnetization transfer from inhomogeneously broadened lines: A potential marker for myelin: Magn. Reson. Med. 73, 614–622. https://doi.org/10.1002/mrm.25174

Varma, G., Girard, O.M., Mchinda, S., Prevost, V.H., Grant, A.K., Duhamel, G., Alsop, D.C., 2018. Low duty-cycle pulsed irradiation reduces magnetization transfer and increases the inhomogeneous magnetization transfer effect. J. Magn. Reson. 296, 60–71. https://doi.org/10.1016/j.jmr.2018.08.004

Varma, G., Girard, O.M., Prevost, V.H., Grant, A., Duhamel, G.D., Alsop, D.C., 2015b. Interpretation of magnetization transfer from inhomogeneously broadened lines (ihMT) in tissues as a dipolar order effect within motion restricted molecules. J. Magn. Reson. 260, 67–76. https://doi.org/10.1016/j.jmr.2015.08.024

Varma, G., Girard, O.M., Prevost, V.H., Grant, A.K., Duhamel, G., Alsop, D.C., 2017. In vivo

measurement of a new source of contrast, the dipolar relaxation time, T1D , using a modified inhomogeneous magnetization transfer (ihMT) sequence. Magn. Reson. Med. 78, 1362–1372. https://doi.org/10.1002/mrm.26523

Wolff, S.D., Balaban, R.S., 1989. Magnetization transfer contrast (MTC) and tissue water proton relaxation in vivo. Magn. Reson. Med. 10, 135–144. https://doi.org/10.1002/mrm.1910100113

Yarnykh, V.L., 2012. Fast macromolecular proton fraction mapping from a single off-resonance magnetization transfer measurement. Magn. Reson. Med. 68, 166–178. https://doi.org/10.1002/mrm.23224

Zaaraoui, W., Deloire, M., Merle, M., Girard, C., Raffard, G., Biran, M., Inglese, M., Petry, K.G., Gonen, O., Brochet, B., Franconi, J.-M., Dousset, V., 2008. Monitoring demyelination and remyelination by magnetization transfer imaging in the mouse brain at 9.4 T. Magn. Reson. Mater. Phys. Biol. Med. 21, 357–362. https://doi.org/10.1007/s10334-008-0141-3

Figure Captions

Fig 1. ***Standard*** **and** ***boosted*** **ihMT protocols**. **a)** ***standard*** and **b)** ***boosted*** ihMT protocols obtained with distributed RF power and concentrated RF power throughout the irradiation period, τ, respectively. Concentration of RF power was achieved using bursts of N_p RF pulses followed by a mixing time without RF power, repeated every B_{TR}. Dashed boxes were zoomed in to display the main features of the RF pulses: Hann-shaped pulses (normalized power integral 0.375), duration PW, pulse repetition time Δt, peak power b_1 (standard protocols) or b_1' (boosted protocols), frequency $+\Delta f$ or $-\Delta f$. MT^{+-} was achieved either by frequency alternation (from $+\Delta f$ to $-\Delta f$), allowing T_{1D}-filtering, or with cosine-modulated pulses (CM, peak power increased by a $\sqrt{2}$ factor), producing simultaneous irradiation at $+\Delta f$ and $-\Delta f$. CM pulses did not allow T_{1D}-filtering. Identical irradiation power, $b_{1,rms}$, was used for all experiments. Note that the indicated $b_{1,rms}$ formulas applied for Hann-shape pulses.

Fig 2. *standard* ihMTR and *boosted* ihMTR (N_p*=12,* B_{TR}*=90ms*) maps obtained on the same mouse for different T_{1D}-filtering strengths at **a)** -3.2mm and **b)** -0.7mm from bregma. Other irradiation parameters were $B_{1,rms}$=6.7μT, Δf=10kHz and τ=900ms. These maps were used for correlation analyses with GFP fluorescence by comparing ihMTR values and normalized GFP intensity measured in ROIs outlined in Fig. 3d.

Fig 3. **(a)** ihMTR maps (*boosted* protocol, N_p*=12*, B_{TR}*=90ms*, weak T_{1D}*-filtering*, Δt*=1.3ms*) with insets showing zoomed regions for comparison with **(b)** GFP fluorescence images. Images located at -0.7mm and -3.2mm from bregma. Note that the bright spots visible at the bottom of the ihMTR map (-3.2mm from bregma) correspond to trigeminal nerves, which were not preserved during the brain extraction. **(c)** Mouse brain atlas at -0.7mm and -3.2mm from bregma indicating the investigated brain structures: cortex (Cx), corpus callosum (CC), thalamus (Th), internal capsule (IC), optic nerves (ON), hippocampus (HC) and Inter-Peduncular Nucleus (IPN). **(d)** ROIs used for quantitative analyses and regression analyses are superimposed on ihMTR maps and GFP fluorescence images.

Fig 4. Linear regressions of ihMTR values derived from the 6 ihMT protocols described in table 1 on myelin density according to $[\overline{GFP}]$ values in brain structures for **(a)** individual measurements in each animal and each ROI of Figs. 3d and **(b)** mean values in each ROI (error bars representing standard deviations across mice). Plain markers correspond to results from *standard* ihMT protocols (Fig.1a) and open markers from *boosted* ihMT protocols (Fig. 1b). The different colors indicate variable T_{1D}-filtering strengths. Linear fits ($ihMTR = \alpha \times [\overline{GFP}] + \beta$) to scatterplot data were obtained by least-square regression and correlation coefficients, r^2, (assessed by a bivariate (Pearson) correlation test) were reported for all protocols. Shaded areas correspond to confidence curves for line fits with a α–level=0.1. All correlations were significant (p <0.0001).

Fig 5: Linear regressions of $MTR^{+\Delta f}$ **(a,b)** and $MTR^{+/-\Delta f}$ **(c,d)** values derived from the 6 protocols described in table 1 on myelin density according to $[\overline{GFP}]$ values in brain structures for **(a, c)** individual measurements in each animal and each ROI of Figs. 3d, and **(b, d)** mean values in each ROI (error bars representing standard deviations across mice). The different colors indicate variable T_{1D}-filtering strengths. Linear fits ($MTR^{+\Delta f} = \alpha \times [\overline{GFP}] + \beta$ **(a,b)** and $MTR^{+/-\Delta f} = \alpha \times [\overline{GFP}] + \beta$ **(c,d)**) to scatterplot data were obtained by least-square regression and correlation coefficients, r^2, (assessed by a bivariate (Pearson) correlation test) were reported for all protocols. Shaded areas correspond to confidence curves for line fits with a α–level=0.1. All correlations were significant (P <0.0001 for $MTR^{+/-\Delta f}$ *v.s.* GFP, and P <0.02 for $MTR^{+\Delta f}$ *v.s.* GFP).

Fig A.1. **Representative *boosted* ihMTR brain images.** IhMTR values and contrasts between structures are modulated by the combined effects of T_{1D}-filtering and the concentration of RF power. Arrows indicate internal capsule (IC, red), cortex (Cx, blue) and muscle (Mu, green). Highly-concentrated RF power (N_p=2) resulted in reduced signal when combined with T_{1D}-filtering **(a)** but in a very large increase without T_{1D}-filtering **(d)**, for which highest ihMTR values were obtained in all brain structures. This highlighted the non-equivalence of frequency-alternated pulses and cosine-modulated pulses for dual-offset irradiation. For less-concentrated RF power, T_{1D}-filtering, **(b)**, allowed better contrast between highly-myelinated WM (e.g. IC) and muscle at the cost of a slight signal decrease compared to that without T_{1D}-filtering, **(c)**.

Fig A.2. Dependence of ihMTR with T_{1D}-filtering and RF power concentration. Variations of ihMTR values measured in Internal Capsule (IC, **(a), (d), (g)**), Cortex (Cx, **(b), (e), (h)**) and muscle (Mu, **(c), (f), (i)**) as a function of the T_{1D}-filtering strength (**(a-c)**, strong T_{1D} -filtering, Δt=3.3ms; **(d-f)**, weak T_{1D}-filtering, Δt=1.3ms; **(g-i)**, no T_{1D}-filtering, *CM*) and the RF power concentration (adjusted by variable values of $\{N_p, B_{TR}\}$, the number of pulses per burst and the burst repetition time). ihMTR values derived from optimized *standard* ihMT protocols were taken from (Prevost et al., 2017)

Fig A.3. Numerical simulations of the dependence of ihMTR with RF power concentration with and without T_{1D}-filtering. A piecewise numerical integration of the ihMT theory (Mchinda et al., 2017; Varma et al., 2015b) was implemented using a MATLAB solver (ode45) and the methodology described in (Mchinda et al., 2017) adapted to the ihMT-prepared *boosted* sequence (i.e. simulating the *boosted* ihMT RARE sequence used experimentally) instead of an ihMT-steady-state *boosted* sequence (i.e. simulating the *boosted* ihMT-GRE sequence). Simulations considered the following tissue parameters, adapted from literature (Mchinda et al., 2017):

$$T_{1A} = 0.65s,\ R = 65\text{s}^{-1},\ f = 0.65\ ,\ T_{2B} = 12.5\ \mu\text{s},\ 1/(R_{1A}T_{2A}) = 581\ ,\ RM_{0B}/R_{1A} = 7.3$$

Simulations are shown for T_{1D} values of 6.2ms (mimicking Internal capsule case) **(a,b)** and 1.0ms (mimicking muscle) **(c,d)** with weak T_{1D}-filtering **(a,c)** and without T_{1D}-filtering **(b,d)**. RF power concentration was varied with changes in $\{N_p, B_{TR}\}$ values.

Fig A.4. Numerical simulations of MT^{+} and $MT^{+/-}$. Variations of MT^{+} (grey curves) and MT^{+-} (achieved with frequency-alternated pulses (yellow curves) and cosine-modulated pulses (orange curves)) with B_{TR} are shown for N_P=2 **(a)** and N_P=12 **(b)**. T_{1D} was set to 6.2ms for both cases. This figure explains the different behavior of frequency-alternated pulses and cosine-modulates pulses for dual irradiation at high RF power concentration, at the origin of the opposed variations of ihMTR for N_P=2 (Fig. A.2d vs Fig. A.2g, and Fig. A.3a vs Fig. A.3b).

Fig B.1. Bland–Altman plots comparing the normalized ihMTR and $[\overline{GFP}]$ values in IC, CC, ON, Th, IPN, Cx and HC ROIs as illustrated in Figs. 3d. Solid and dashed lines correspond to the mean difference and limits of agreement, respectively.

Fig B.2. Bland–Altman plots comparing the normalized $MTR^{+\Delta f}$ and $[\overline{GFP}]$ values **(a)**, as well as the normalized $MTR^{+/-\Delta f}$ and $[\overline{GFP}]$ values **(b),** in IC, CC, ON, Th, IPN, Cx and HC ROIs as illustrated in Figs. 3d. Solid and dashed lines correspond to the mean difference and limits of agreement, respectively.